



**Citation:** Pensalfini M, Tepole AB (2023) Mechanobiological and bio-mechanical pathways in cutaneous wound healing. PLoS Comput Biol 19(3): e1010902. https://doi.org/10.1371/journal.pcbi.1010902

**Editor:** Alison L. Marsden, Stanford University, UNITED STATES

Received: August 2, 2022

Accepted: January 27, 2023

Published: March 9, 2023

Copyright: © 2023 Pensalfini, Tepole. This is an open access article distributed under the terms of the Creative Commons Attribution License, which permits unrestricted use, distribution, and reproduction in any medium, provided the original author and source are credited.

**Data Availability Statement:** All relevant data are within the manuscript and its Supporting information files.

Funding: This work was supported by the Swiss National Science Foundation under award Doc. Mobility P1EZP2\_178376 to MP, and by the US National Science Foundation Civil, Mechanical and Manufacturing Innovation Directorate under award NSF-CMMI 1911346 to ABT. The funders had no role in study design, data collection and analysis, decision to publish, or preparation of the manuscript.

RESEARCH ARTICLE

# Mechano-biological and bio-mechanical pathways in cutaneous wound healing

Marco Pensalfini 1,2,3\*, Adrian Buganza Tepole 1,4\*

- 1 School of Mechanical Engineering, Purdue University, West Lafayette, Indiana, United States of America, 2 Institute for Mechanical Systems (IMES), Department of Mechanical and Process Engineering, ETH Zurich, Zurich, Switzerland, 3 Laboratori de Càlcul Numèric (LaCàN), Universitat Politècnica de Catalunya-BarcelonaTech, Barcelona, Spain, 4 Weldon School of Biomedical Engineering, Purdue University, West Lafayette, Indiana, United States of America
- \* mpensalf@alumni.purdue.edu (MP); abuganza@purdue.edu (ABT)

#### **Abstract**

Injuries to the skin heal through coordinated action of fibroblast-mediated extracellular matrix (ECM) deposition, ECM remodeling, and wound contraction. Defects involving the dermis result in fibrotic scars featuring increased stiffness and altered collagen content and organization. Although computational models are crucial to unravel the underlying biochemical and biophysical mechanisms, simulations of the evolving wound biomechanics are seldom benchmarked against measurements. Here, we leverage recent quantifications of local tissue stiffness in murine wounds to refine a previously-proposed systems-mechanobiological finite-element model. Fibroblasts are considered as the main cell type involved in ECM remodeling and wound contraction. Tissue rebuilding is coordinated by the release and diffusion of a cytokine wave, e.g. TGF-β, itself developed in response to an earlier inflammatory signal triggered by platelet aggregation. We calibrate a model of the evolving wound biomechanics through a custom-developed hierarchical Bayesian inverse analysis procedure. Further calibration is based on published biochemical and morphological murine wound healing data over a 21-day healing period. The calibrated model recapitulates the temporal evolution of: inflammatory signal, fibroblast infiltration, collagen buildup, and wound contraction. Moreover, it enables in silico hypothesis testing, which we explore by: (i) quantifying the alteration of wound contraction profiles corresponding to the measured variability in local wound stiffness; (ii) proposing alternative constitutive links connecting the dynamics of the biochemical fields to the evolving mechanical properties; (iii) discussing the plausibility of a stretch- vs. stiffness-mediated mechanobiological coupling. Ultimately, our model challenges the current understanding of wound biomechanics and mechanobiology, beside offering a versatile tool to explore and eventually control scar fibrosis after injury.

# **Author summary**

Wounds constitute a major healthcare burden, often yielding overly stiff scars that feature altered collagen content and organization. Accurate computational models have the potential to impact the understanding, treatment, and ultimately the outcome of wound

**Competing interests:** The authors declare no competing interests.

healing progression by highlighting key mechanisms of new tissue formation and providing a versatile platform for hypothesis testing. However, the description of wound biomechanics has so far been based on measurements of uninjured tissue behavior, limiting our understanding of the links between wound stiffness and healing outcome. Here, we leverage recent experimental data of the local stiffness changes during murine wound healing to inform a computational model. The calibrated model also recapitulates previously-measured biochemical and morphological aspects of wound healing. We further demonstrate the relevance of the model towards understanding scar formation by evaluating the link between local changes in tissue stiffness and overall wound contraction, as well as testing hypotheses on: (i) how local tissue stiffness is linked to composition; (ii) how a fibrotic response depends on mechanobiological cues.

#### Introduction

Caused by a variety of possible conditions, including surgeries, traumas, and pathologies, wounding of the skin triggers a well-coordinated repair program that aims to rebuild the damaged tissue and recover its function via biological, chemical, and physical events [1]. Classical descriptions of healing progression consider three overlapping but distinct stages [2, 3]: inflammation, proliferation, and remodeling. Inflammation begins immediately after injury, when a coagulation cascade attracts platelets to the injury site [1, 3]. Their rapid aggregation in a crosslinked fibrin mesh results in a blood clot, a provisional scaffold for inflammatory cell migration [1, 3, 4]. Platelet aggregation and degranulation triggers the release of various chemokines, including platelet-derived growth factor (PDGF), vascular endothelial growth factor (VEGF), transforming growth factor beta (TGF- $\beta$ ), and tumor necrosis factor alpha (TNF- $\alpha$ ) [1, 2, 4, 5]. These play a key role in recruiting neutrophils, which are the first inflammatory cells to infiltrate the wound and contribute to fight pathogens and avoid infection [2, 4]. A second wave of inflammatory cells involves monocyte migration, driven by chemoattractants such as monocyte chemotactic protein 1 (MCP-1) [2] and TGF- $\alpha$ [5]. Monocytes differentiate primarily into macrophages [2, 3, 5], which amplify earlier wound signals by releasing growth factors such as PDGF, VEFG, TGF-β, and fibroblast growth factors (e.g. FGF-2) [1, 2, 6]. The growth factor profiles established by macrophages coordinate tissue rebuilding during the proliferation phase, which occurs through the activity of various cell types [3, 7]. Keratinocytes are the first to intervene, crawling over the injured tissue in the process of epithelialization to restore the skin barrier function [2, 3]. Within angiogenesis, endothelial cells contribute to form new blood vessels [2, 5]. Fibroblasts have a key role in rebuilding the dermis—the collagen-rich layer mainly responsible for the skin structural function [8, 9]—by producing and organizing the extracellular matrix (ECM) that ultimately forms the bulk of the mature scar [3, 10], in a process stimulated by TGF-β, PDGF, and FGF-2 [5] and facilitated by cell-mediated secretion of proteolytic enzymes termed matrix metalloproteinases (MMPs) [2]. PDGF and TGF-β are also key mediators of fibroblast differentiation into myofibroblasts [5], a contractile cell phenotype that tends to approximate wound edges. Both cell types exert active stresses on the surrounding ECM and regulate collagen remodeling [2, 3], which contribute to determine the geometry and mechanical properties of the scar together with externally-applied tissue deformations [7, 11, 12]. Lastly, remodeling is a long-term process characterized by downregulation of overall cellular activity, cell population density, and collagen remodeling [3, 5].

Defects involving the dermis result in scars that lack the organization and full functionality of unwounded skin, exhibiting excessive stiffness, reduced strength, and permanent

contracture that can persist for months or even years [10, 13–15]. This represents a significant healthcare burden, with an estimated cost per wound requiring treatment of about \$4'000 in the US [16] and an annual management cost over £5 billion in the UK [17]. Several exogenous agents, such as medications [18], environmental conditions [19], and mechanical loading [7], may negatively affect wound healing. Fibroblast differentiation, migration, and gene expression pathways is widely acknowledged to depend on biomechanical cues [20–22]. Indeed, clinical evidence demonstrates reduction of hypertrophic scar formation via disruption of relevant mechanobiological pathways [23, 24] or by modulating local tissue tension [25, 26]. Moreover, negative-pressure therapy can accelerate the healing of chronic wounds through a process involving macroscopic deformations of the wound bed [27, 28], shock waves can enhance tissue vascularization, collagen synthesis, and cell proliferation [28], and ultrasounds can stimulate granulation via tissue cavitation [28]. While these mechanotherapies can influence the course and outcome of healing, their working principles remain elusive due to insufficient understanding of the corresponding biophysical phenomena [22].

Owing to the complexity of tissue repair processes, computational models have become key tools to study the interplay of biological, chemical, and physical events, as well as to formulate and test hypotheses by providing access to quantities that are otherwise hard to determine [29]. The first computational models date back to the 1990s and mainly focused on the dynamics of cell populations, described with either ordinary [30, 31] or partial [32] differential equations (ODEs or PDEs, respectively) or with agent based models [33]. Further developments incorporated wound contraction by imposing conservation of collagen density and linear momentum for the ECM [34], including myofibroblast contributions [35, 36]. However, these models often featured a simplistic description of mechanics, leading to a superficial treatment of the pathways linking cell behavior to mechanical cues. We and others have been interested in incorporating detailed representations of tissue mechanics into wound healing models. Bowden et al.[37] proposed a purely mechanical model including tissue growth, while our most recent approaches [38–40] couple basic biochemical fields with tissue nonlinear mechanics, including permanent changes in shape and stiffness that result from growth and remodeling. Importantly, all these models adopt mechanical constitutive parameters that are representative of uninjured skin, strongly limiting their relevance towards investigating the link between ECM biomechanics and the outcome of healing.

Here, we set out to overcome this limitation by leveraging one of the very few available experimental datasets on the time-course evolution of wound mechanics at physiological deformation levels, which have been recently measured on murine tissue by Pensalfini *et al.* [41]. Through a custom-developed hierarchical Bayesian calibration procedure, we establish the change in mechanical behavior during healing, and use the calibrated constitutive model to refine our systems-mechanobiological finite-element (FE) model of wound healing. We further leverage the versatility of our model to test hypotheses regarding the link between tissue composition and evolving tissue stiffness, as well as the role of mechanobiological coupling to trigger fibrosis.

## Materials and methods

# Systems-mechanobiological model of wound healing

The 2D Lagrangian FE model that we use is publicly available [42] and follows closely our original formulation [39]. Here, we briefly state the main equations and modeling assumptions, both for completeness and to reflect changes from our previous work. Note that this is a general formulation, which can also be implemented in a 3D solver. For details regarding the weak form, FE discretization, assembly of residual and tangents, and code verification, we refer the reader to Ref. [39].

**Kinematics and modeled fields.** Following standard continuum mechanics notation, the current tissue geometry is described by the coordinates x. The reference configuration, X, coincides with the initial tissue geometry in its  $ex\ vivo$ , unloaded state. Wound healing is simulated starting from an intermediate state,  $x^{i.v.}$ , accounting for  $in\ vivo$  skin pre-tension. Local deformation is captured by the deformation gradient tensor,  $F = \partial x/\partial X$ .

Motivated by the overview provided in the Introduction, we model the biochemical fields by grouping the release of pro-inflammatory cytokines into two waves [1-6]. The first signal,  $\alpha$ , is triggered upon platelet aggregation and helps direct inflammatory cells such as neutrophils and macrophages towards the wound bed. The second wave, c, represents the growth factors and cytokines that coordinate and regulate tissue rebuilding and remodeling via fibroblasts and myofibroblasts. Being mainly interested in new tissue formation and remodeling, we limit our description of inflammation to the fields  $\alpha$  and c, avoiding explicit modeling of the corresponding cell species. Accordingly, the cell population density,  $\rho$ , coincides with the amount of fibroblasts/myofibroblasts in the tissue, owing to their widely-recognized role towards determining ECM deposition and organization in wounds and scars. Similar modeling assumptions have been previously adopted in the literature [32, 36-39]. Lastly, the tissue composition is mainly described by its collagen content,  $\phi_c$ , and by the plastic deformation,  $F^p$ , which reflects on the permanent stretch ratios,  $\lambda_a^p$  and  $\lambda_s^e$ , measured along the in-plane eigenvectors of  $\mathbf{F}^p$ ,  $\mathbf{a}_0$  and  $\mathbf{s}_0$ . Note that we take the values of c,  $\rho$ ,  $\phi_c$ ,  $\lambda_a^p$ , and  $\lambda_s^p$  in an unwounded tissue subjected to a physiological deformation level to be 1, while  $\alpha = 0$  in such conditions. Normalization of biochemical fields is common in systems biology modeling when absolute concentrations are difficult to obtain, see for example the modeling frameworks in Refs. [31, 32, 34].

**Balance laws for mass and linear momentum.** The balance of linear momentum follows the standard relation  $\nabla \cdot \boldsymbol{\sigma} = \mathbf{0}$ , where  $\boldsymbol{\sigma}$  denotes the Cauchy stress tensor and is determined by two contributions:

$$\boldsymbol{\sigma} = \boldsymbol{\sigma}^{act} + \boldsymbol{\sigma}^{pas}. \tag{1}$$

In Eq (1),  $\sigma^{act}$  is the active stress exerted by the cell population,  $\rho$ , on the collagenous ECM,  $\phi_c$ , influenced by two factors, cf. Eqs (11 and 12) and Fig 1: (i) the mechanical state of the wound; (ii) the cytokines c. The passive stress,  $\sigma^{pas}$ , only depends on the mechanical state of the tissue via Eq (2), cf. Fig 1. Contractile stress by (myo)fibroblasts has been also included in other wound healing models [29, 32, 34–39], as well as to capture the remodeling of tissue engineered constructs [40, 43].

The balance of mass for the *diffusible* biochemical fields  $\alpha$ , c, and  $\rho$  follows standard equations. For instance, the second inflammatory signal must satisfy the relation  $\dot{c} + \nabla \cdot \mathbf{q}_c = s_c$ , where  $s_c$  and  $\mathbf{q}_c$  are the source and flux terms in the current configuration, respectively. In the Lagrangian setting, the flux of c is expressed by  $\mathbf{Q}_c = J\mathbf{F}^{-1}\mathbf{q}_c$ , where  $J = \det \mathbf{F}$ .

The tissue microstructural fields,  $\phi_c$ ,  $\lambda_a^p$ ,  $\lambda_s^p$ , are updated locally and without accounting for any diffusion; their rate of change is defined later on, along with the corresponding constitutive equations.

Constitutive equations for the tissue mechanical behavior. The passive stress in the tissue derives purely from the elastic part of the deformation gradient tensor  $F^e = FF^{p-1}$  and is assumed to follow from a hyperelastic potential similar to the one used in the Gasser-Ogden-Holzapfel (GOH) model [44]:

$$\Psi(\mathbf{F}^{e}) = C_{10} \left( I_{1}^{e} - 3 \right) + \frac{k_{1}}{2k_{2}} \left\{ \exp \left[ k_{2} \left( \frac{I_{1}^{e}}{3} - 1 \right)^{2} \right] - 1 \right\}, \tag{2}$$

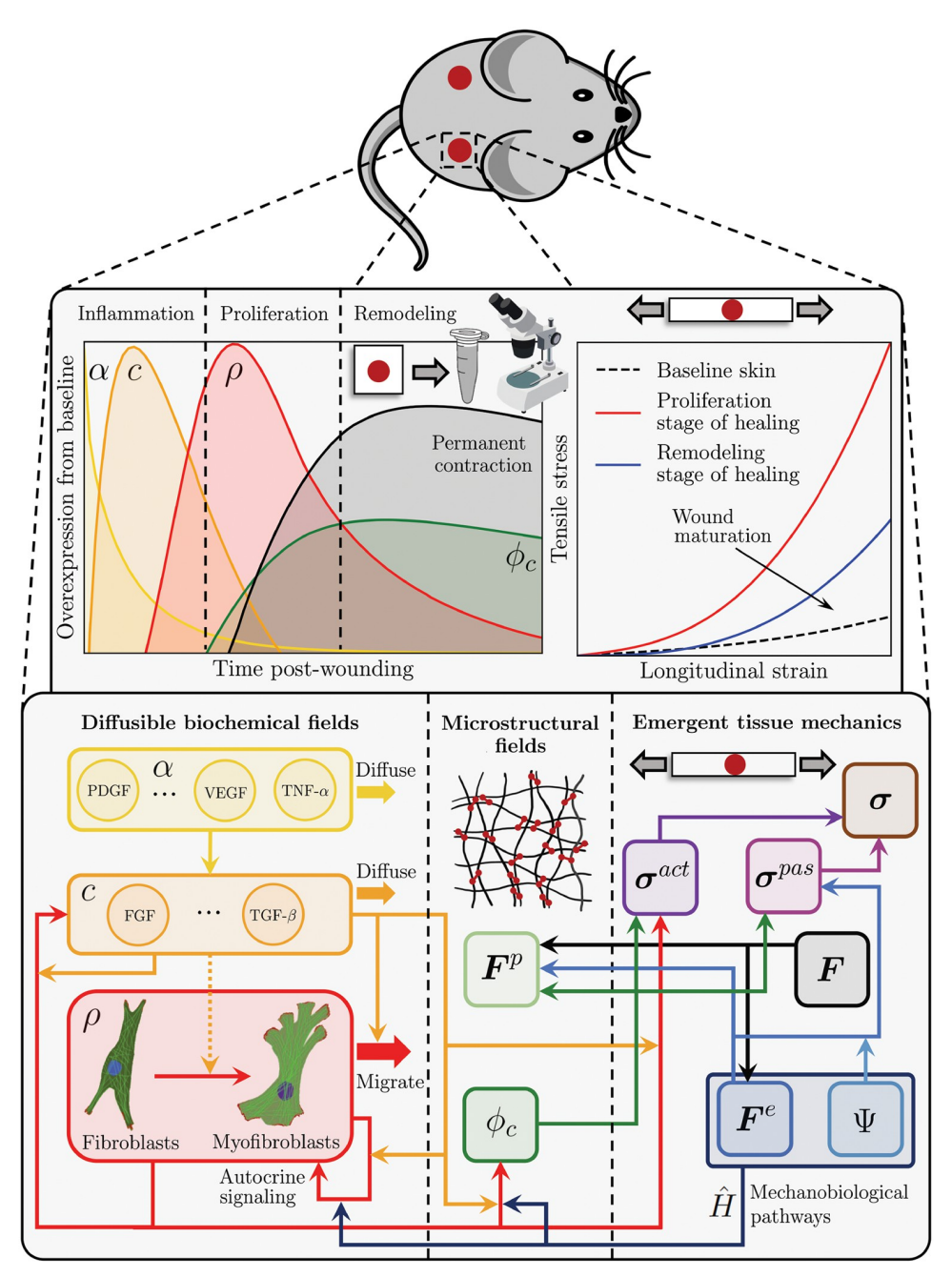


Fig 1. Schematic summarizing the developed systems-mechanobiological model of wound healing, which aims to capture the temporal evolution of key biochemical, microstructural, and macroscopic mechanical and geometrical variables by representing the cell and tissue regulatory pathways and their interaction across structural scales. Images used in this figure were downloaded from Labicons.net and openclipart.org.

where  $I_1^e = \operatorname{tr}(\boldsymbol{C}^e)$  is the first invariant of the elastic right Cauchy-Green deformation tensor,  $\boldsymbol{C}^e = \boldsymbol{F}^{e\top} \boldsymbol{F}^e$ , and  $C_{10}$ ,  $k_1$ ,  $k_2$  are material parameters. This constitutive model describes the characteristic J-shaped stress-strain response observed in many soft biological tissues [44–49] by assuming a neo-Hookean ground substance with shear modulus  $\mu_0 = 2C_{10}$  and a collagen-based network whose emergent stiffening upon stretching is controlled by the phenomenological parameters  $k_1$  and  $k_2$ . Note that we consider a simplified model with respect to the original formulation [44], by assuming that skin and wound/scar tissues are isotropic materials subjected to plane stress conditions, since the modeled skin region has thickness much smaller than its in-plane dimensions.

Constitutive equations for the diffusible biochemical fields. The fluxes of  $\alpha$ , c, and  $\rho$  in the reference configuration are expressed by:

$$\mathbf{Q}_{\alpha} = -J D_{\alpha,\alpha} \mathbf{C}^{-1} \nabla_{X} \alpha,$$

$$\mathbf{Q}_{c} = -J D_{c,c} \mathbf{C}^{-1} \nabla_{X} c,$$

$$\mathbf{Q}_{\rho} = -J (D_{\rho,\rho} \mathbf{C}^{-1} \nabla_{X} \rho + D_{\rho,c} \mathbf{C}^{-1} \nabla_{X} c),$$
(3)

where  $\mathbf{C} = \mathbf{F}^{\top} \mathbf{F}$ , and  $D_{\alpha,\alpha}$ ,  $D_{c,c}$ ,  $D_{\rho,\rho}$ ,  $D_{\rho,c}$  are diffusion coefficients.

Since inflammatory cell recruitment is mostly completed within the first few days after injury [5], we assume an exponentially-decaying source term for  $\alpha$ , with rate  $d_{\alpha}$ :

$$s_{\alpha} = -d_{\alpha} \alpha. \tag{4}$$

The source term for the second inflammatory wave, c, accounts for its dependence on the first inflammatory wave,  $\alpha$ , and on the fibroblast/myofibroblast population density,  $\rho$ :

$$s_c = p_{c,\alpha} \alpha + p_{c,\rho} \langle c_{tgt} - c \rangle \frac{\rho}{K_{c,c} + c} - d_c c, \tag{5}$$

where  $c_{tgt}$  is an attractor for c and is selected to ensure homeostasis of this biochemical field for an unwounded tissue subjected to physiological deformation, while  $\langle \rangle$  denote the Macauley brackets that prevent the second term on the right-hand side of Eq.(5) from becoming negative when  $c > c_{tgt}$ .  $K_{c,c}$  determines the saturation of c in response to itself,  $p_{c,\alpha}$  and  $p_{c,\rho}$  are coefficients capturing the effects of  $\alpha$  and  $\rho$  on the release of cytokines, c, (Fig.1), and  $d_c$  is the decay rate when all production terms are zero. Similar forms for inflammatory reaction-diffusion systems can be found in Refs. [30, 34, 38, 39].

The source term for  $\rho$  is an extension of logistic models with cytokine feedback and mechanobiological coupling, see for example Refs. [34, 50], and is purely a reformulation of our previous works [39, 40]:

$$s_{\rho} = \rho \left[ p_{\rho,n} \left( 1 + \Omega_{\rho}^{b} \frac{c}{K_{\rho,c} + c} + \Omega_{\rho}^{m} \hat{H}_{\rho} \right) \left( 1 - \frac{\rho}{K_{\rho,\rho}} \right) - d_{\rho} \right]. \tag{6}$$

The function  $\hat{H}_{\rho}$  encodes the dependence of fibroblast/myofibroblast proliferation on the mechanical state of the tissue (Fig 1), as discussed in more detail below.  $p_{\rho,n}$  defines the natural mitotic rate of the cells in the absence of cytokines and mechanical effects (c=0,  $\hat{H}_{\rho}=0$ ), while  $\Omega_{\rho}^{b}$  and  $\Omega_{\rho}^{m}$  are coefficients capturing the enhanced cell proliferation in response to c and  $\hat{H}_{\rho}$  (Fig 1).  $K_{\rho,c}$  and  $K_{\rho,\rho}$  determine the saturation of  $\rho$  in response to c and to itself, and  $d_{\rho}$  is again the decay rate when all production terms are set to zero. We select  $d_{\rho}$  to ensure that  $\rho$  respects homeostasis for an unwounded tissue subjected to physiological deformation.

Constitutive equations for the tissue microstructural fields. The tissue microstructure changes in two ways during wound healing: one of them is the change in composition, *e.g.* the collagen mass fraction  $\phi_c$ , and the other is the change in permanent deformation,  $\mathbf{F}^p$ , which depends on the permanent stretch ratios,  $\lambda_a^p$  and  $\lambda_s^p$ .

Similar to our previous works [39, 40], and supported by other computational models of remodeling in biological tissue [35, 36], we assume that  $\phi_c$  depends linearly on the fibroblast/myofibroblast population density,  $\rho$ , in a way that is mediated by c (Fig 1):

$$\dot{\phi}_{c} = \dot{\phi}_{c}^{+} - \dot{\phi}_{c}^{-} = 
= p_{\phi_{c},n} \left( 1 + \Omega_{\phi_{c}}^{b} \frac{c}{K_{\phi_{c},c} + c} + \Omega_{\phi_{c}}^{m} \hat{H}_{\phi_{c}} \right) \frac{\rho}{K_{\phi_{c},\rho} + \phi_{c}} - \left( d_{\phi_{c}} + \rho \, c \, d_{\phi_{c},\rho,c} \right) \phi_{c}.$$
(7)

The function  $\hat{H}_{\phi_c}$  encodes the dependence of cell-mediated collagen deposition on the mechanical state of the tissue (Fig 1). Similar mechanobiological couplings have been used in [36, 39, 50]. For simplicity, we set  $\hat{H}_{\rho} = \hat{H}_{\phi_c} = \hat{H}$ , i.e. we assume that mechanical cues impact cell proliferation and collagen deposition in the same fashion up to a scaling factor,  $\Omega_{\rho}^m$  vs.  $\Omega_{\phi_c}^m \cdot p_{\phi_c,n}$  defines the natural rate of collagen deposition in the absence of cytokines and mechanical effects (c=0,  $\hat{H}_{\phi_c}=0$ ), while  $\Omega_{\phi_c}^b$  and  $\Omega_{\phi_c}^m$  are coefficients capturing the enhanced collagen deposition in response to  $\rho$  and  $\hat{H}_{\phi_c} \cdot K_{\phi_c,c}$  and  $K_{\phi_c,\rho}$  determine the saturation of  $\phi_c$  in response to c and to c0. Note that, beside a spontaneous decay mediated by the coefficient  $d_{\phi_c}$ , selected to ensure homeostasis of  $\phi_c$  in unwounded physiological conditions, the collagen degradation rate ( $\phi_c$ ) also depends on  $\rho$  and c via  $d_{\phi_c,\rho,c}$ , capturing the role of cells within MMP production [2] and the corresponding modulation by cytokines [51].

Lastly, the remodeling law operates independently along the principal directions  $a_0$  and  $s_0$  according to the equation (Fig 1):

$$\lambda_a^{\dot{p}} = \dot{\lambda}_s^{\dot{p}} = \begin{cases}
\frac{\dot{\phi}_c^+}{\tau_{\lambda^p}} (\lambda^e - 1), & \text{if } \lambda^e \leq 1, \\
0, & \text{if } 1 < \lambda^e < \sqrt{9^{ph}}, \\
\frac{\dot{\phi}_c^+}{\tau_{\lambda^p}} (\lambda^e - \sqrt{9^{ph}}), & \text{if } \lambda^e \geq \sqrt{9^{ph}},
\end{cases}$$
(8)

where  $\lambda^e$  is the current elastic stretch of the tissue along the direction of interest,  $\tau_{\lambda P}$  is the time constant for tissue growth in either direction, and  $\vartheta^{ph}$  captures the elastic areal deformation of the tissue in its physiological *in vivo* state. Different from our previous approaches [38–40], but in line with the concept that cells respond to environmental cues to maintain homeostasis [52], Eq.(8) implies that the tissue grows when stretched past its physiological state, shrinks when subjected to prolonged compression, but accumulates no permanent deformation when stretched to sub-physiological levels. Given the permanent stretches  $\lambda^p_a$ ,  $\lambda^p_s$ , the permanent deformation tensor is assumed of the form

$$\mathbf{F}^p = \lambda_a^p \mathbf{a}_0 \otimes \mathbf{a}_0 + \lambda_a^p \mathbf{s}_0 \otimes \mathbf{s}_0. \tag{9}$$

**Mechano-biological and bio-mechanical pathways.** The modeled biochemical fields can determine (bio→mechanics) and be determined (mechano→biology) by the mechanical state

of the tissue ECM in multiple ways (Fig 1). A first relevant bio-mechanical pathway has been discussed in the previous section: plastic deformation is influenced by collagen turnover, itself a function of cell activity. Plastic deformation also dissipates elastic energy, affecting tissue deformation,  $F^e$ . This has then a mechano-biological effect on the cell population and collagen deposition, as mediated by the function  $\hat{H}$ , cf. Eqs (6 and 7). A leading hypothesis in the field, which we have also used previously [39, 40], postulates a dependence of  $\hat{H}$  on strain:

$$\hat{H} = \hat{H}(\theta^e, \vartheta^{ph}, \gamma^e) = \frac{1}{1 + \exp[-\gamma^e(\theta^e - \vartheta^{ph})]},\tag{10}$$

where  $\theta^e = \|\cos \mathbf{F}^e \cdot \mathbf{N}\|$  captures the current in-plane elastic tissue deformation, while  $\gamma^e$  controls the slope of  $\hat{H}$  around its midpoint,  $\vartheta^{ph}$ . While the majority of this manuscript adopts Eq (10), we will also explore an alternative coupling as part of our hypothesis testing efforts, cf. Results.

A further bio-mechanical pathway of interest is represented by cell-induced contraction, yielding an active tension that depends on  $\rho$  and c (Fig 1):

$$f(\rho,c) = \left(1 + \Omega_f^b \frac{c}{K_{f,c} + c}\right) \rho f_{\rho,n}. \tag{11}$$

In the above expression, which is purely a reformulation of what we have previously used [39, 40],  $f_{\rho,n}$  is the baseline tension exerted by a physiological population of fibroblasts/myofibroblasts on the surrounding ECM in the absence of any cytokine ( $\rho = 1$ , c = 0),  $\Omega_f^b$  captures the tension increase in response to c, e.g. due to enhanced fibroblast-myofibroblast transition, and  $K_{f,c}$  determines the saturation of f in response to c. The active stress resulting from the tension introduced in Eq. (11) reads:

$$\boldsymbol{\sigma}^{act} = \phi_c f(\rho, c) \frac{\boldsymbol{b}}{\operatorname{tr}(\boldsymbol{b})}, \tag{12}$$

where  $b = FF^{\top}$ . Note that, owing to the assumption of tissue isotropy, the current expression for active stress is simplified with respect to our previous approach [39], which adopted a deformed structural tensor based on a direction of anisotropy.

#### Hierarchical Bayesian calibration of mechanical parameters

To determine the constitutive parameters of unwounded and wounded tissues at various healing time points, we leverage the experimental measurements previously presented in Pensalfini *et al.* [41], where several specimens including a 7- or 14-day-old wound were subjected to *ex vivo* uniaxial tensile tests and compared to the mechanical response of unwounded skin. Contrary to most traditional material parameter-fitting approaches, which either focus on the average measured mechanical response for a set of homogeneous specimens [48, 53, 54], or treat each tested specimen completely independently [46, 48, 55, 56], here we develop a novel hierarchical Bayesian calibration procedure.

Consider a generic mechanical constitutive model that can be specified by prescribing an m-tuple of parameters,  $\mu = (\mu_1, \ldots, \mu_m)$ , providing a deterministic relation between applied deformation, e.g. the stretch  $\lambda$ , and stress:  $P = P(\mu, \lambda)$ . We wish to determine values of  $\mu$  yielding the experimentally-measured stresses for each of the  $N_s$  specimens at time points  $\bar{t}$ . We denote each parameter set as  $\mu^{(J)}(\bar{t}) = (\mu_1^{(J)}(\bar{t}), \ldots, \mu_m^{(J)}(\bar{t}))$ , with  $J = 1, \ldots, N_s$ . Since wound infliction and progression are the main factors determining the mechanical parameters, we reason that all  $\bar{t}$ -old parameters can be regarded as originating from a common probability

distribution. To restrict the mechanical constitutive parameters to be non-negative, we assume that  $\mu_{\bar{i}}^{(J)}(\bar{t})$  originate from a log-normal distribution,

$$\mu_i(\bar{t}) = \exp[\log(\alpha_{\mu_i}) + \sigma_{\mu_i}\tilde{\mu}_i] = \alpha_{\mu_i}\exp(\sigma_{\mu_i}\tilde{\mu}_i), \tag{13}$$

where  $\tilde{\mu_i} \sim \mathcal{N}(0,1)$  is a normally-distributed variable  $(\mathcal{N})$  with zero mean and unit variance, while  $\log(\alpha_{\mu_i})$  and  $\sigma_{\mu_i}$  are the expected value and standard deviation of  $\mu_i(\bar{t})$ 's natural logarithm. Importantly,  $\log(\alpha_{\mu_i})$  and  $\sigma_{\mu_i}$  are not fixed values, but they also originate from distributions (Fig 2), highlighting the *hierarchical* (or nested, or multilevel) structure of the posed statistical model, where the moments of the mechanical parameter distributions are themselves obtained from distributions. To stress the generating role of  $\log(\alpha_{\mu_i})$ ,  $\sigma_{\mu_i}$ , and  $\mathcal{N}(0,1)$  with respect to  $\mu_i(\bar{t})$ , we refer to the former as *hyperdistributions*. In the absence of more detailed

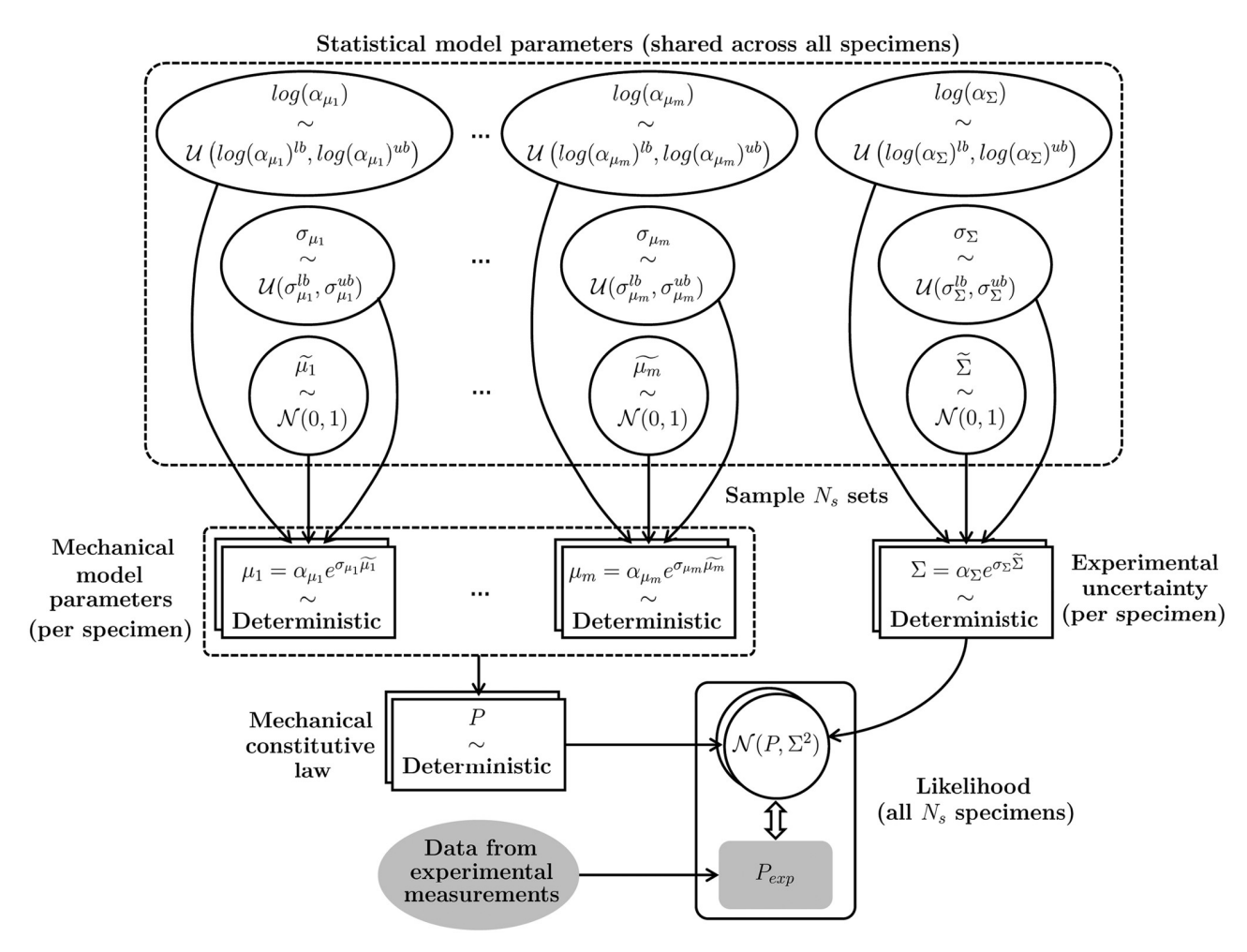


Fig 2. Schematic of the hierarchical Bayesian model posed to capture the experimentally-measured mechanical response of a set of  $N_s$  interrelated tissue specimens. A set of 3(m+1) hyperdistributions, common across all specimens, generates the  $mN_s$  mechanical model parameters corresponding to each tested specimen, and the  $N_s$  parameters representing experimental uncertainty. These parameters yield deterministic predictions for the mechanical behavior of each specimen, which are to be compared to the corresponding experimental evidence in order to establish a best-fitting set of hyperparameters.

https://doi.org/10.1371/journal.pcbi.1010902.g002

information, we will assume uniform hyperdistributions ( $\mathcal{U}$ ) one for each value of the subscript i:  $\log(\alpha_{\mu_i}) \sim \mathcal{U}(\log(\alpha_{\mu_i}^{lb}), \log(\alpha_{\mu_i})^{ub})$  and  $\sigma_{\mu_i} \sim \mathcal{U}(\sigma_{\mu_i}^{lb}, \sigma_{\mu_i}^{ub})$ . Thus, each independent sampling of the hyperdistributions  $\log(\alpha_{\mu_i})$ ,  $\sigma_{\mu_i}$ , and  $\mathcal{N}(0,1)$  generates, via Eq.(13), one value for the i-th entry of the m-tuple of mechanical parameters,  $\mu_i^{(J)}(\bar{t})$ . In turn, the mechanical constitutive model yields  $P = P(\mu^{(J)}(\bar{t}), \lambda)$  (Fig.2), and the experimental measurement process introduces further uncertainty, which we model as Gaussian noise,  $\mathcal{N}(P, \Sigma^2)$ .

We are interested in the *inverse* relation, from the experimental measurements to the parameters,  $\Theta$ . In Bayesian terms, the hierarchical model prescribes the *likelihood*  $p(\mathcal{N}(P,\Sigma^2)\mid\Theta)$ , *i.e.* the probability distribution of the observed data given a set of parameters, and we wish to determine the *posterior*  $p(\Theta|P_{\text{exp}})$ , *i.e.* the probability distribution of the parameters given the data,  $P_{\text{exp}}$ . According to Bayes' theorem:

$$p\left(\Theta \mid P_{exp}\right) \approx p\left(\Theta \mid \mathcal{N}\left(P, \Sigma^{2}\right)\right) = \frac{p(\mathcal{N}(P, \Sigma^{2}) \mid \Theta)p(\Theta)}{\int_{\Theta} p(\mathcal{N}(P, \Sigma^{2}) \mid \Theta)p(\Theta) d\Theta}, \tag{14}$$

where  $p(\Theta)$  is the *prior*, *i.e.* the probability distribution of the parameters  $\Theta$  before any observation has been made, and  $\int_{\Theta} p(\mathcal{N}(P,\Sigma^2) \mid \Theta) p(\Theta) d\Theta$  is the *evidence*, a normalization factor coinciding with the probability distribution of the observed data independently from any parameter set.

To determine the posterior without computing the evidence, it is possible to resort to numerical methods such as Markov Chain Monte Carlo (MCMC) or Variational Inference (VI) [57]. A key difference between the two approaches is that MCMC assumes no model for the posterior, while VI casts inference as an optimization problem and seeks the best approximant of the posterior within a parameterized family of distributions according to a suitable cost function, e.g. the Kullback-Leibler divergence, or a likelihood function, e.g. the Evidence Lower Bound (ELBO) [57]. This allows reducing the variance of the method at the cost of introducing some bias, such that VI approaches are generally less accurate than MCMC but tend to be faster and scale better to large datasets [57]. Given the complexity of our hierarchical model and the fairly large datasets that we aim to fit, featuring thousands of experimental data points, we adopt a VI approach and specify the model using the Python-based probabilistic programming framework PyMC3 [58]. Specifically, we adopt a gradient-based approach known as Automated Differential Variational Inference (ADVI) [59] and assume that the posterior follows a spherical Gaussian distribution without correlation of parameters, which we estimate by maximizing the ELBO [58]. The corresponding code is publicly available [42].

#### Wound healing simulations

To simulate wound healing *in vivo*, we start from a square skin patch with side length 50 mm in its reference state (Fig 3a and S1 Video), and set its mechanical constitutive parameters according to the median values obtained from Bayesian calibration. To limit the computational cost, we restrict our model to 1/4 of the considered patch and impose symmetric boundary conditions on x = 0 and y = 0 (cf. Fig 3 and S1 Video).

We approximate *in vivo* pre-tension by subjecting the unwounded tissue to an equibiaxial stretch with  $\lambda_x = \lambda_y = 1.15$  (Fig 3b and S1 Video), which is within the broad range of previously-reported post-excisional skin shrinkage values [56, 60, 61]. Following equilibration, we introduce a wound by setting the constitutive parameters  $C_{10}$  and  $k_1$  in a 5 mm-diameter tissue region located at the center of the computational domain to extremely small values,  $C_{10}^{i.w.} = 0.0$  kPa and  $k_1^{i.w.} = 0.0$  MPa (*i.w.*: immediately after wounding), while leaving  $k_2$ 

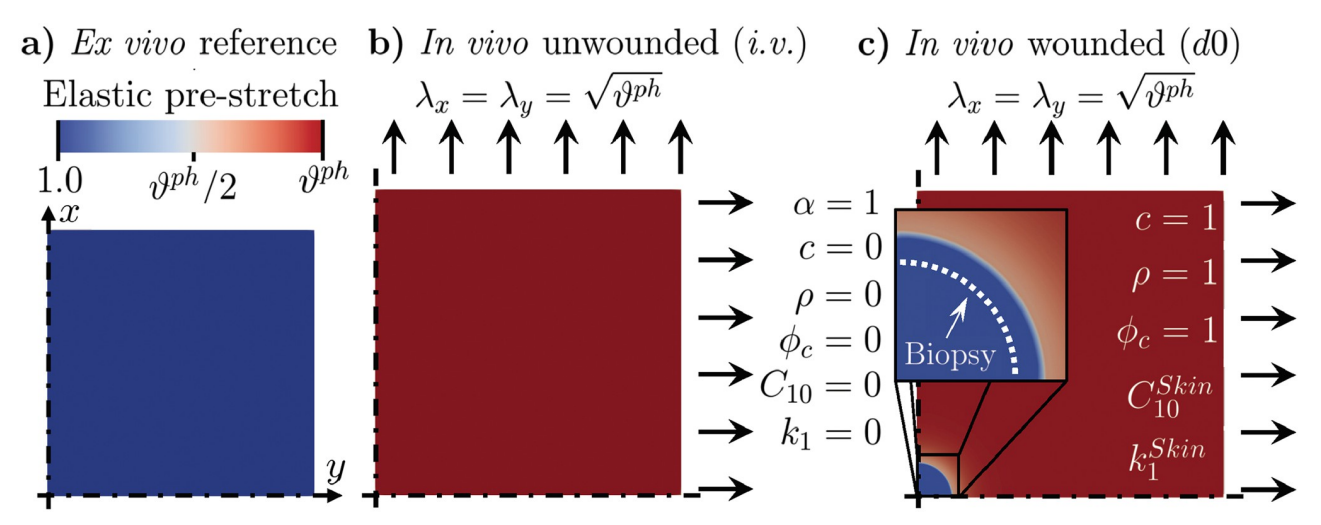


**Fig 3. Model preparation before solving the wound healing problem.** (a) Modeled square tissue patch, with symmetric boundary conditions along x = 0 and y = 0 and mechanical constitutive parameters corresponding to unwounded skin. (b) Unwounded skin patch in its *in vivo* state (*i.v.*), characterized by an equi-biaxial pre-stretch. (c) Wound infliction *in vivo*, obtained by setting the mechanical parameters in a circular tissue region to extremely small values; the values of the biochemical and microstructural quantities ( $\alpha$ , c,  $\rho$ ,  $\phi_c$ ) are also adjusted to reflect a freshly-wounded tissue. Note that, immediately after infliction, the wound enlarges due to the corresponding release of tissue pre-stretch, as shown in the inset (white dashed line vs. boundary of the blue region). The reached deformation is made permanent to ensure that the newly-deposited tissue has no initial stress.

unchanged. Owing to the stark contrast between the mechanical properties of the wound and those of the surrounding skin, this causes the wound region to expand (inset in Fig 3c and S1 Video), much like the classical problem of a membrane featuring a circular hole and subjected to tension. Shortly after infliction, at time point d0 (day 0 of the healing time-course, Fig 3c), we also impose that the wound exhibits a peak in the first inflammatory wave ( $\alpha^{d0} = 1$ ), which is associated with platelet aggregation, and negligible values for the second inflammatory wave ( $c^{d0} = 0$ ), cell density ( $\rho^{d0} = 0$ ), and collagen content ( $\phi_c^{d0} = 0$ ). Meanwhile, all biochemical and microstructural variables in the surrounding skin have physiological values:  $\alpha^{Skin,d0} = 0$ ,  $\rho^{Skin,d0} = 1$ , and  $\phi_c^{Skin,d0} = 1$ . Lastly, since no collagen deposition can occur prior to day 0, we assume that the fibrin clot ensures tissue integrity and linearly extrapolate the value of  $C_{10}^{d0} > C_{10}^{l.w.}$ , while we set  $k_1^{d0} = k_1^{l.w.}$ .

Starting from d0, we conducted several numerical investigations simulating the wound healing time-course, backed up by an extensive literature review to determine reasonable values for the parameters controlling the temporal evolution of the biochemical fields and wound area. In a first set of simulations, we fixed the evolution of the mechanical parameters  $C_{10}$ ,  $k_1$ ,  $k_2$  inside and outside of the wound for times  $t \in [0, 21]$  days according to the results of Bayesian calibration, and found that tuning the value of 5 parameters was sufficient to match available experimental data on the dynamics of the biochemical fields and of the wound area, cf. S3 and S4 Tables. With this calibrated model, we then set to test constitutive equations linking the biochemical fields to the measured change in mechanics. First, we used previously proposed constitutive relations for  $\dot{C}_{10}(c,\rho,\phi_c)$  and  $\dot{k}_1(\alpha,c,\rho,\phi_c)$ , and found that they were unable to capture the data accurately, cf. Results. We thus proposed alternative constitutive relations, obtaining a model that is able to reproduce the evolution of the biochemical fields as well as the change in mechanics without the need for any prescribed field, *i.e.* entirely from the constitutive and balance equations. With this refined model, we were in the position to ask questions regarding the mechanobiological feedback, and we altered Eq (10) to test the ability of both a

stretch-driven and a stiffness-driven coupling towards describing the wound tendency to exhibit hypertophic scarring due to mechanobiological pathways [23, 24].

#### Results

# Evolution of wound mechanical behavior throughout healing

To determine GOH constitutive parameters describing the tensile experiments performed in Ref. [41], we focus on each of the three available datasets and conduct separate parameter optimizations for the unwounded skin specimens ( $N_s = 8$ ), the 7-day-old wounds ( $N_s = 8$ ), and the 14-day-old wounds ( $N_s = 8$ ). For simplicity of analysis, we focus on the wound core regions identified in Ref. [41] and assume that they were subjected to uniaxial tensile loading, neglecting any possible influence of the surrounding tissue on the measured response. We also assume a tissue thickness of 1.7 mm, in line with [10].

For each of the three separate parameter optimizations, we train the hierarchical model with 200'000 samples by prescribing fairly broad search ranges, cf. S1 Table, and ensuring convergence of the ELBO, cf. S1 Fig. We then use the calibrated statistical models to generate 10'000 independent samples to get the  $N_s$  = 8 posterior distributions of the mechanical parameters  $C_{10}$ ,  $k_1$ , and  $k_2$ , one per specimen, along with the priors, traces, and posteriors of the hyperparameters (S2, S3 and S4 Figs). For simplicity, Fig 4a, 4b and 4c only shows the median values of the specimen-specific mechanical parameter posteriors (dots), along with boxplots indicating the corresponding median (orange line), interquartile range (box), and the 95% confidence interval (CI, indicated by the extension of the whiskers). Remarkably, the posterior of the constitutive parameter  $k_2$ , which mainly controls tissue stiffening at large stretches, can only be inferred for the unwounded specimens (Fig 4c and S2 Fig), which are indeed those consistently reaching the largest deformations (Fig 4d vs. Fig 4e and 4f). Instead, for the wounded specimens, we fix  $k_2$  = 0.88 according to the median of the specimen-specific posteriors obtained for unwounded skin (Fig 4c) and restrict our analysis to the parameters  $C_{10}$  and  $k_1$ .

Despite the large variability in the inferred mechanical parameters, which is certainly not unexpected when quantifying the properties of biological materials, the adopted hierarchical model provides information on each tested specimen, allowing us to discuss the evolution of  $C_{10}$  and  $k_1$  throughout healing. On the one hand,  $C_{10}$ , whose median value across 7-day-old specimens is about 2.2× the one of unwounded skin, reaches about 1/20 of the unwounded value at day 14, showing a 42.5× reduction. Instead,  $k_1$  is consistently larger in the wounds (11.9× at day 7, 5.6× at day 14) than in the unwounded skin specimens, despite a 2.1× reduction between days 7 and 14. Since the GOH model uses  $k_1$  to capture the stiffening of the collagenous ECM, the evolution of this parameter can be interpreted as indicative of pronounced and sustained tissue fibrosis in the wound/scar with respect to the unwounded tissue. Concomitantly, the GOH model parameter  $C_{10}$ , capturing the mechanical contribution of the noncollagenous ground substance, also appears significantly affected by wound healing progression, suggesting marked softening of this tissue component.

Lastly, we access the calibrated statistical model traces to visualize the tensile curve posteriors. For each specimen, we randomly generate 1'000 curves that account for experimental uncertainty, as captured by the modeling parameter  $\Sigma$ , and confirm that the 95% CI of the model-based predictions match the experimental measurements (Fig 4d, 4e and 4f). Thus, the determined constitutive parameters capture the tensile response of the tissue specimens, suggesting that they can be used to infer the mechanical changes in the wounded skin throughout healing.

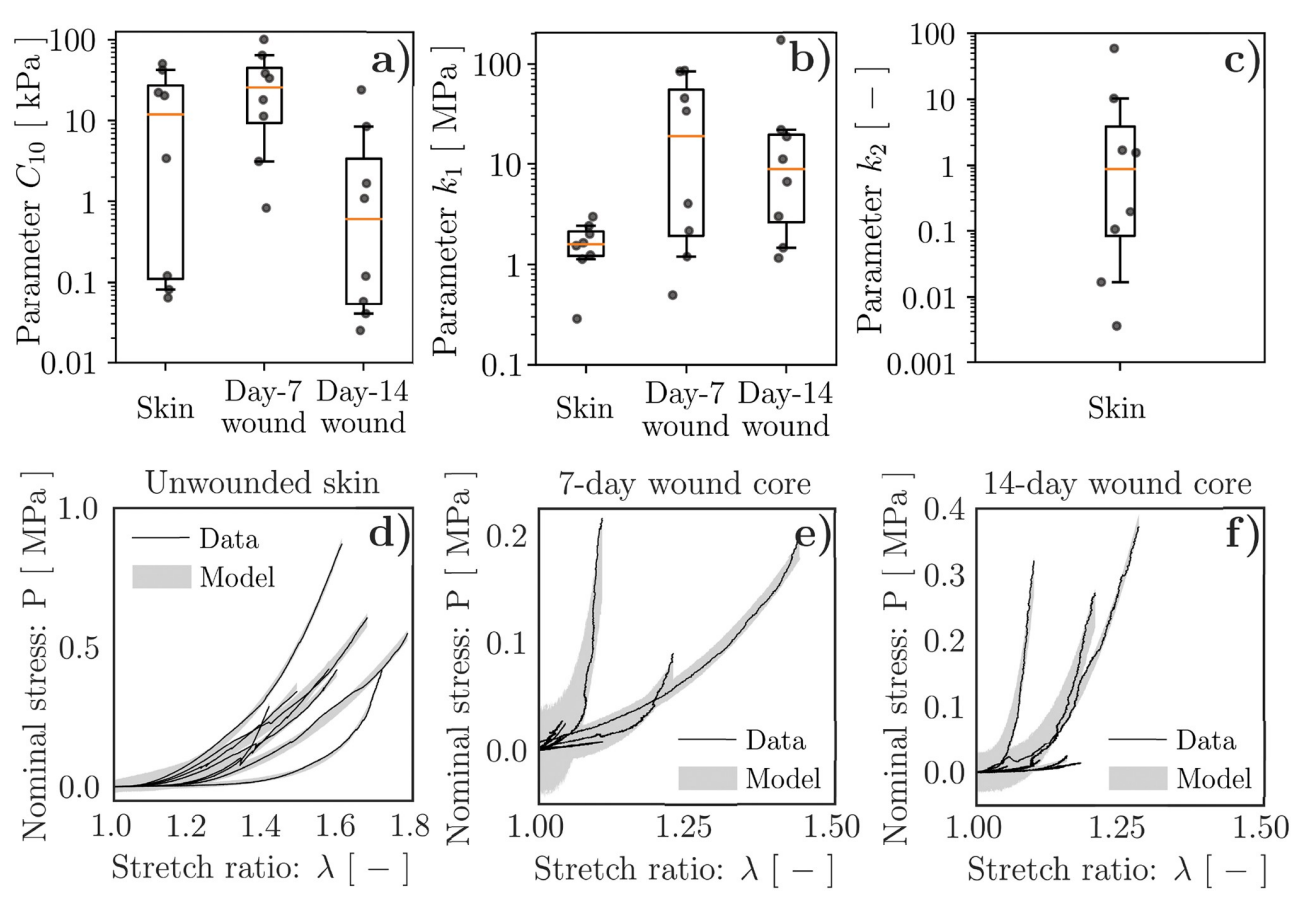


**Fig 4. Hierarchical Bayesian calibration of tissue mechanical parameters.** (a)  $C_{10}$ , corresponding to the behavior of the non-collagenous ground substance, exhibits marked decrease between 7- and 14-days post-wounding, while mostly remaining within the broad range of values characterizing unwounded skin. (b)  $k_1$ , corresponding to the behavior of the tissue collagenous matrix, tends to decrease between 7- and 14-days post-wounding, and is typically larger in the wounds than in unwounded skin. (c)  $k_2$ , relating to the large deformation behavior of the tissue collagenous matrix, can only be inferred for unwounded skin due to the limited deformability of wounded tissues prior to failure. (d-f) Model-based predictions of the specimen tensile behavior accounting for experimental uncertainty. The dots in (a-c) indicate median values of the parameter posteriors for each of the  $N_s$  = 8 specimens, cf. S2, S3 and S4 Figs. The boxplots in (a-c) are constructed based on the values indicated by the dots, with orange lines denoting the median and extension of the whiskers denoting the 95% CI. The shadings in (d-f) indicate the 95% CI obtained from 1'000 random tensile curves generated using the calibrated Bayesian model and accounting for experimental uncertainty.

## Influence of wound deformability on the healing outcome

Having established plausible ranges and trends for the mechanical constitutive parameters of wounded and unwounded tissues, we aim to investigate their influence on the evolution and outcome of healing over 21 days, a common time span for murine studies. To this end, we assign the mechanical parameters according to the lower bound (2.5<sup>th</sup> percentile), median values, or upper bound (97.5<sup>th</sup> percentile) obtained from Bayesian calibration, assuming linear variation between their known or estimated values at days 0, 7, and 14, and no variation between days 14 and 21 (Fig 5a and 5b and S1 Video, and S5 Table). Conversely, the parameters controlling the temporal evolution of the biochemical fields and wound area are fixed in time and determined based on an extensive literature review of the available data on the amount of cytokines [62–65], cells [62, 66], and collagen [67–70] in murine wounds, as well as on stretch-dependent fibroblast proliferation [71], *cf.* S3 and S4 Tables, and S1 Appendix. Specifically, some parameters are directly determined from published experimental values, *e.g.* the

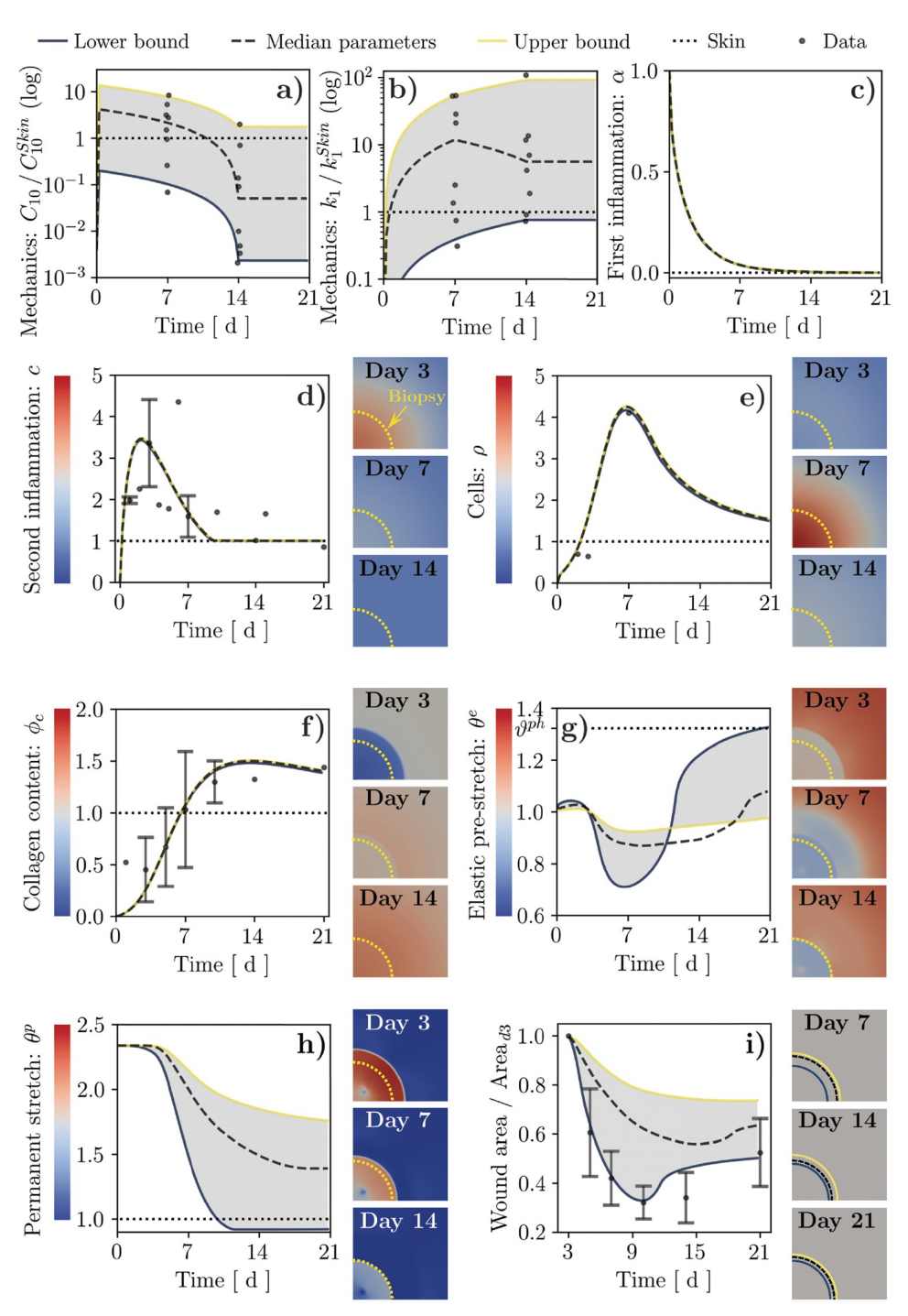


Fig 5. Results of wound healing simulations over a 21-day period using the wound mechanical parameters directly obtained from the Bayesian calibration procedure (median and 95% CI) and assuming linear variation between known or estimated values. (a, b) Hard-coded time evolution of the mechanical parameters  $C_{10}/C_{10}^{\rm Skin}$  and  $k_1/k_1^{\rm Skin}$ , along with the corresponding values from Bayesian calibration (dots, cf. Fig 4). (c) Decay of the first inflammatory signal,  $\alpha$ , in the wound. (d-h) Time and spatial evolution of: second inflammatory signal, c; cell population,  $\rho$ ; tissue collagen content,  $\phi_c$ ; tissue elastic stretch,  $\theta^e$ ; tissue plastic stretch,  $\theta^e$ . (i) Time evolution and illustration of wound area changes. Dots and error bars in (d,e,f,i): mean  $\pm$  standard deviation of previously-published experimental data, cf. S1 Appendix and Ref. [10].

fold increase in collagen deposition in response to inflammatory cytokines, while others are taken from our previous work [39] and references therein. Additionally, 3 parameters ( $c_{tg}$ ,  $d_{\rho}$ ,  $d_{\phi_c}$ ) are computed based on others to ensure that the source terms in Eqs (5–7) vanish under unwounded physiological conditions, *i.e.* to respect homeostasis constraints. Ultimately, only 5 parameters ( $p_{c,co}$ ,  $K_{\rho,c}$ ,  $K_{\rho,\rho}$ ,  $\Omega^b_{\rho_c}$ ) are directly calibrated using the FE model in order to match specific features of the temporal evolutions of biochemical parameters, *e.g.* the supraphysiological peak in cell population, and recent data on changes in the visible wound area [10]. All model parameters are reported in the Supporting information, cf, S2–S5 Tables.

In our simulations, irrespective of the imposed constitutive parameters,  $\alpha$  simply decays exponentially to zero over 7–10 days (Fig 5c and S1 Video) as prescribed by Eq (4). Similarly, c increases from its initial value of 0 to a maximum of about 3.5× at day 2–3 post-wounding, before returning to its physiological value of 1 in a way that is also largely independent of mechanics (Fig 5d and S1 Video). The contours to the right of the chart in Fig 5d show the spatial variation of c over time. As expected from the dependence of c on  $\alpha$  (Eq (5)), and based on the role of diffusion, the profiles for c exhibit a peak at the center of the wound in the early stages of healing (days 0–3), which diffuses smoothly into the surrounding tissue over time (days 3–7).

The cell density,  $\rho$ , exhibits a peak of about 4.2× around day 7 post-wounding, followed by gradual decay over time (Fig 5e and S1 Video). The entire evolution of  $\rho$  lags behind that of c, as also visible in the corresponding contour plots. This delay originates from both fibroblast chemotaxis (Eq (3)) and increased proliferation (Eq (6)) in response to c. Fibroblasts infiltrating the wound have a key role in depositing collagen, one of the main microstructural fields in the current model, leading its content to gradually increase starting from day 7 post-wounding. Remarkably, the collagen content in the wound peaks at a value of 1.4–1.5×, which is first reached around day 10 and persists until day 21 (Fig 5f and S1 Video). Note that, while  $\rho$  and  $\phi_c$  depend on the mechanical deformation of the tissue (Eqs (6 and 7)), varying the mechanical constitutive parameters according to the determined 95% CI has almost no influence on Fig 5e and 5f. This counterintuitive finding will be discussed in a later section.

The other main microstructural field that we quantify from the FE simulations is the plastic deformation,  $\theta^p = \lambda_s^p \lambda_s^p$  (Fig 5h), which is governed by Eq (8) and is intimately related to the elastic deformation,  $\theta^e$  (Fig 5g). Shortly after injury, the wound void is enlarged up to reaching  $\theta^{e, i.w.} \approx 2.3$  due to *in vivo* pre-tension, and then filled by a fibrin clot made of a virgin material. After setting  $\theta^p = \theta^{e, i.w.}$  to ensure absence of initial stress, the elastic deformation in the clot is initially 1 (no deformation). Elastic deformation is affected both by the active stress applied by the infiltrating fibroblasts and by the growth/shrinkage of the wound tissue (Eq (8)). Notably,  $\theta^e < 1$  for the majority of wound healing progression, leading to a progressive decrease in the plastic deformation (Fig 5h and S1 Video) and a corresponding decrease in the wound area (Fig 5i). Note that, unlike the amount of elastic or plastic deformation in the wound, wound area is typically measured in wound healing experiments, allowing our model to be compared to quantitative data such as those presented in Ref. [10].

Remarkably, the temporal evolution of the fields directly associated with deformation is strongly influenced by the constitutive behavior of the wound ECM, and both the plastic deformation and wound area are smaller/larger for softer/stiffer ECMs. When the wound ECM is softer than the surrounding skin for the majority of the healing time-course (lower bound curves in Fig 5), the infiltrating cells can easily contract the wound, resulting in a strong initial decrease in elastic deformation  $\theta^e$ —until a minimum of about 0.7 around day 7—that yields a drastic reduction in  $\theta^p$ , as prescribed by Eq (8). Around day 14, with the downregulation of the active stress  $\sigma^{act}$ , the tissue approaches its physiological elastic deformation,  $\vartheta^{ph}$ .

Conversely, when the wound ECM is consistently stiffer than the surrounding tissue (median and upper bound curves in Fig 5), the effect of the active stresses on the wound deformation is mitigated, resulting in a more modest reduction of  $\theta^p$  during the early stages of healing. In this case,  $\theta^e$  never approaches  $\theta^{ph}$  when the active stresses are subsequently reduced.

The present wide-range model calibration allows recapitulating the temporal evolution of several key aspects of wound healing, such as infiltration of cytokines and fibroblasts, collagen deposition, as well as the size and deformation of a developing scar. As such, our model offers a versatile platform to address the plausibility of alternative hypotheses concerning the biomechanical and mechanobiological pathways involved in wound healing.

# Linking the wound mechanical behavior to tissue microstructure

Having established a reliable model of wound progression, we now aim to propose plausible links between the emergent mechanical behavior of the healing tissue and the microstructural fields that, in turn, depend on the biochemical fields. Hence, we turn our attention to replacing the hard-coded evolution of wound mechanical properties by constitutive hypotheses. Collagen being among the major determinants of soft tissue biomechanics [8], a common approach in the literature [36, 72–75]—which we have also previously followed [39, 40]—is to make  $k_1$  proportional to  $\phi_c$ . In addition, our material parameter calibration indicated a clear reduction of the value of  $C_{10}$ , capturing the mechanical behavior of the tissue non-collagenous ground substance, throughout healing (Fig 4a). Accordingly, we posit that  $C_{10}$  might represent the mechanical contribution of the fibrin clot that is formed at the onset of the healing response and is gradually depleted by the infiltrating cells via fibrinolytic enzymes and MMPs [5]. Thus, we introduce a microstructural field encoding the wound fibrin content,  $\phi_f^w$ , and assume a purely decaying temporal evolution mimicking that of collagen:

$$\dot{\phi_f^w} = -(d_{\phi_f^w} + \rho \, c \, d_{\phi_f^w, \rho, c}) \, \phi_f^w, \tag{15}$$

Note that the microstructural field  $\phi_f^w$  is specific to the wound, hence the superscript w. In Eq (15),  $d_{\phi_f^w}$  defines the extent of spontaneous fibrin decay and  $d_{\phi_f^w,\rho,c}$  defines the magnitude of cell-mediated fibrin depletion, which we assume to be affected by c in line with the overall modulation of cell activity by cytokines and with previous computational models including multiple chemical species promoting cell-mediated degradation of specific ECM proteins [33]. Here, we set  $d_{\phi_f^w} = d_{\phi_c}$  and choose  $d_{\phi_f^w,\rho,c}$  to ensure that most fibrin decays prior to day 7 (Fig 6c). Similar to the classical link between  $k_1$  and  $\phi_c$ , we also assume proportionality of  $C_{10}^w$  to  $\phi_f^w$ , leading to the following relations between tissue mechanics and microstructure:

$$C_{10}^{w} = \phi_{f}^{w} C_{10}^{Clot, d0},$$
 (16)  
 $k_{1} = \phi_{c} k_{1}^{Skin}.$ 

In Eq (16),  $C_{10}^{Clot, d0}$  is the value of  $C_{10}$  in the wound right after the blood clot has formed, such that  $C_{10}^w = C_{10}^{Clot, d0}$  when  $\phi_f^w = 1$  and  $C_{10}^w = 0$  when  $\phi_f^w = 0$ . Conversely,  $C_{10}$  in the surrounding unwounded tissue is assumed constant throughout healing and set equal to the baseline skin value ( $C_{10} = C_{10}^{Skin}$ ). On the other hand,  $k_1^{Skin}$  is the value of  $k_1$  for an unwounded tissue, such that  $k_1 = k_1^{Skin}$  when  $\phi_c = 1$  (physiological value).

To address the plausibility of the constitutive hypotheses in Eqs (15 and 16), we simulate the evolution of  $C_{10}$  and  $k_1$  throughout wound healing (*cf.* S2 Video), in relation to the

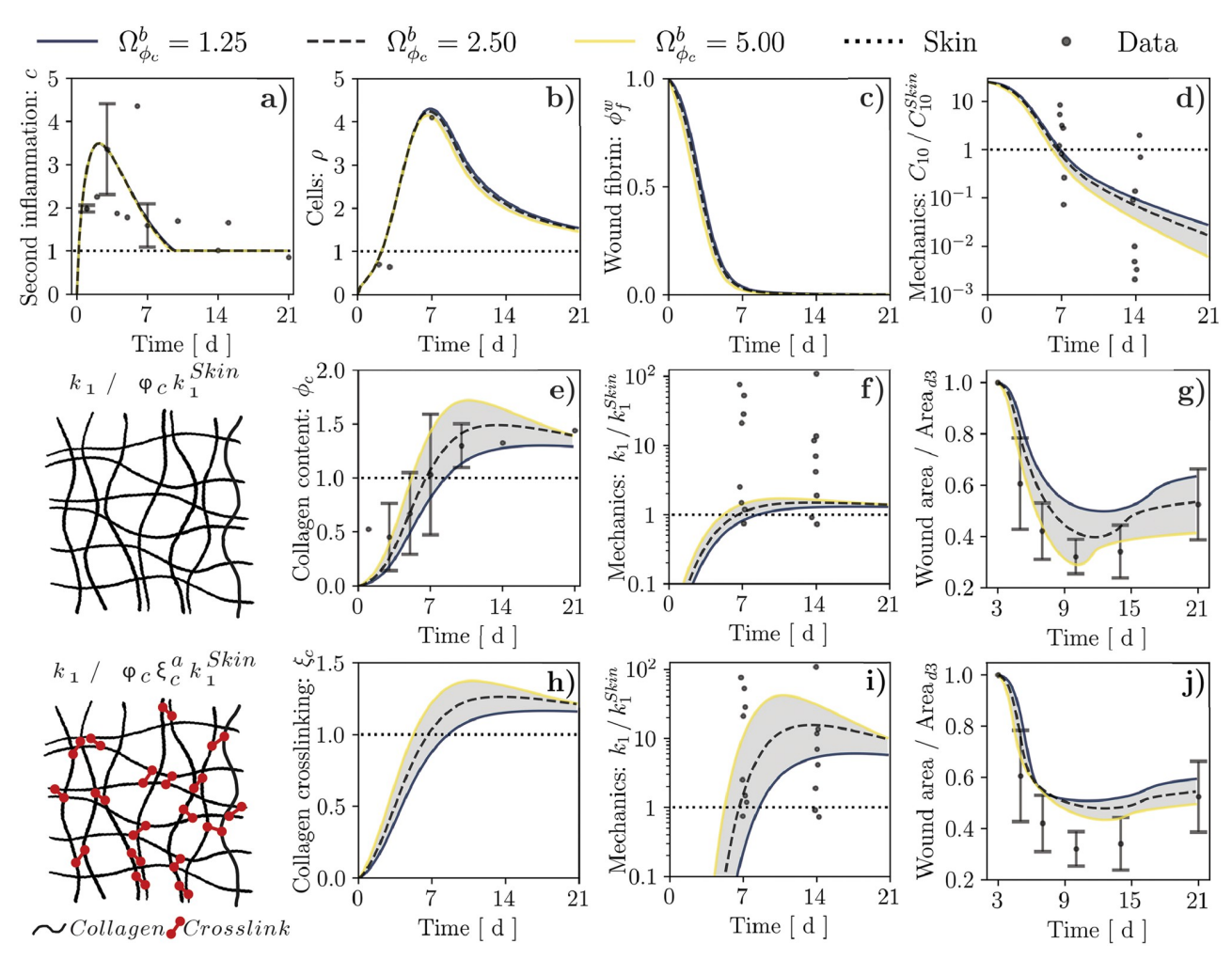


Fig 6. Results of wound healing simulation over a 21-day period for alternative links between the tissue collagen content,  $\phi_c$ , and the mechanical parameter  $k_1$ , and alternative values of the parameter  $\Omega_{\phi_c}^b$  that controls collagen production by cells. (a–d) Temporal evolution of second inflammatory signal, c, cell population,  $\rho$ , wound fibrin content,  $\phi_f^w$ , and mechanical parameter  $C_{10}/C_{10}^{Skin}$  for either considered constitutive link. These quantities do not depend explicitly on  $\phi_c$ , hence we report them only once. (e–g) Temporal evolution of tissue collagen content,  $\phi_c$  mechanical parameter  $k_1/k_1^{Skin}$ , and wound area change resulting from assuming that  $k_1$  is proportional to  $\phi_c$ . (h–j) Temporal evolution of collagen crosslinking,  $\xi_c$ , mechanical parameter  $k_1/k_1^{Skin}$ , and wound area change resulting from assuming that  $k_1$  depends nonlinearly on  $\phi_c$  via  $\xi_c$ . Dots and error bars in (a,b,e,g,j): mean  $\pm$  standard deviation of previously-published experimental data, c. S1 Appendix and Ref. [10]. Dots in (d,f,i): values of  $C_{10}/C_{10}^{Skin}$  and  $k_1/k_1^{Skin}$  obtained from Bayesian calibration, c. Fig 4.

respective baseline values,  $C_{10}^{Skin}$  and  $k_1^{Skin}$ . Notably, selecting  $C_{10}^{Clot, d0}=300\,$  kPa, which is in line with previously-reported shear modulus values for venous thrombi [76], allows capturing the experimentally-informed evolution of  $C_{10}/C_{10}^{Skin}$  in the wound (Fig 6d), supporting a dependence on  $\phi_f^w$ . Conversely, the strong increase in  $k_1$  throughout healing, which we inferred from Bayesian parameter calibration, is not adequately captured by a proportional dependence on  $\phi_c$ . Indeed, even when varying the parameter  $\Omega_{\phi_c}^b$  in the range of 0.5–2.0× to account for possible variability in collagen production (Fig 6e), the predicted values of  $k_1$  hardly exceed the unwounded baseline (Fig 6f). Importantly, this limitation does not affect the model ability to represent the temporal evolution of the diffusible fields c (Fig 6a) and  $\rho$  (Fig 6b), or its ability to capture visible wound area changes (Fig 6g).

Based on the inadequacy of a proportional link between  $k_1$  and  $\phi_c$ , we hypothesize that this constitutive relation should additionally account for the progressive maturation of the newly-formed collagen network. Indeed, alterations in the degree and type of crosslinking have been reported to affect the emergent mechanical behavior of soft tissues such as tendons [77], uterine cervix [78], and skin wounds [10]. For simplicity, we focus on the degree of network crosslinking and consider a nonlinear relation between  $k_1$  and  $\phi_c$ , mediated by a crosslinking agent,  $\xi_c$ :

$$k_1 = \phi_c \, \xi_c^a \, k_1^{\text{Skin}},\tag{17}$$

where  $a \ge 1$  is a phenomenological exponent controlling the degree of tissue nonlinearity associated with a given crosslinking. To prescribe the temporal evolution of  $\xi_c$ , which constitutes an additional microstructural field in our model, we reason that crosslink formation should be positively correlated with  $\phi_c$  since a higher collagen content should provide increased opportunities for physico-chemical interactions, and that the degree of network crosslinking cannot increase indefinitely with  $\phi_c$  but should exhibit a saturating behavior given the finite size of crosslinks. On the other hand, the amount of crosslinks could be reduced spontaneously, as a consequence of stochastic unbinding [79], or indirectly, via depletion of some fibers within the ECM [80]. Accordingly, we express the source term for  $\xi_c$  as:

$$\dot{\xi}_c = \frac{p_{\xi_c,\phi_c}}{K_{\xi_c,\phi_c} + \xi_c} \phi_c - \left( d_{\xi_c} + d_{\xi_c,\dot{\phi}_c} - \dot{\phi}_c^- \right) \xi_c, \tag{18}$$

where  $p_{\xi_c,\phi_c}$  defines the natural forward rate of collagen crosslinking,  $K_{\xi_c,\phi_c}$  determines the saturation of  $\xi_c$  in reponse to  $\phi_c$ ,  $d_{\xi_c}$  is the spontaneous decay rate for crosslinks, selected to ensure homeostasis of  $\xi_c$  in unwounded physiological conditions, and  $d_{\xi_c,\phi_c}$  defines the relation between collagen fiber depletion and the associated crosslink depletion, which relates to the average number of crosslinks per collagen fiber.

Under the constitutive hypotheses in Eqs (17 and 18), collagen crosslinking increases concomitantly with  $\phi_c$  during wound healing, from its initial value of 0 at the onset of wound healing to a supra-physiological value of 1.1–1.4× (depending on the value of  $\Omega_{\phi_c}^b$ ) that is mostly preserved throughout days 10–21 post-wounding (Fig 6h). Selecting a value a=10 for the exponent in Eq (17) allows our model to capture the strong increase and subsequent stabilization of  $k_1$  during the proliferation and remodeling stages of healing (Fig 6i), while continuing to recapitulate previously-measured changes in the visible wound area (Fig 6j). Importantly, the temporal evolution of the diffusible biochemical fields, of the fibrin content, and of the mechanical parameter  $C_{10}$  in the wound are largely unaffected by the assumed link between  $k_1$  and  $\phi_c$  (cf. S3 Video), since the only possible dependence of these quantities on  $k_1$  is through the mechanical deformation of the wounded tissue, which we have already established to have a minor influence on  $\rho$  and  $\phi_c$  in our model. Also note that the nonlinear relation between  $k_1$  and  $\phi_c$  results in an increased sensitivity of  $k_1$  to the modeling parameter  $\Omega_{\phi_c}^b$  (Fig 6i vs. Fig 6f), allowing us to ascribe at least part of the experimental variability in  $k_1$  to potential specimenspecific differences in terms of collagen content and its degree of crosslinking.

#### A closer look at mechano-biological signals: Stretch vs. stiffness

Thus far, we have discussed the influence of wound deformability on the healing outcome and linked the emergent mechanical parameters to the biochemical and microstructural fields. In both cases, we have assumed that cell proliferation and collagen deposition depend on the elastic tissue deformation, as measured by  $\theta^e$ , via the function  $\hat{H}$ . Selecting the parameters of  $\hat{H}$ 

according to our previous works [39, 40] and to match available experimental data on the influence of stretching on fibroblast proliferation [71] yielded a surprisingly modest sensitivity of  $\rho$  and  $\phi_c$  on  $\theta^e$ , cf. Fig 5e and 5f. Since fibroblasts are known to be mechanosensitive, we now turn our attention to the mechano-biological pathway that links cell function to the mechanical state of the ECM. Specifically, we progressively increase the strength of this coupling to test its effect. Note that, for each considered value of  $\Omega^m$ , we also adjust the coefficients  $c_{tgt}$ ,  $d_\rho$ , and  $\phi_c$  so that physiological homeostasis is achieved in the unwounded tissue.

Surprisingly, increasing the value of  $\Omega^m = \Omega^m_{\rho} = \Omega^m_{\phi}$  in Eqs (6 and 7) appears to strongly mitigate fibrosis, leading to a marked decrease in  $\rho$ ,  $\phi_c$ , and  $\xi_c$  (Fig 7b, 7d and 7e). In turn, reduced cell infiltration mitigates the active stresses and the corresponding elastic pre-stretch in the wound ( $\theta^e$ , cf. Fig 7c), leading to decreased area reduction over time (Fig 7f). Slower cell infiltration in the wound also delays fibrin degradation, resulting in a slower decay for C<sub>10</sub> (Fig 7g). Concomitantly, the reduction in  $\phi_c$  and  $\xi_c$  determines a marked decrease in  $k_1$  (Fig 7h), which does not even reach the unwounded baseline value when the mechano-biological feedback is increased to  $\Omega^m = 0.8$ , cf. S4 Video. Moreover, the emergent mechanical behavior of mature scar tissue (day 21 post-wounding) under uniaxial tensile conditions, evaluated analytically using Eq (2), appears significantly softer with larger  $\Omega^m$  (Fig 7i). Taken together, these results indicate that positing a primary dependence of cell activity on ECM deformation might not allow capturing the onset of scar fibrosis. Importantly, this result follows from imposing an initially stress-free fibrin clot, implying an initially much smaller elastic deformation in the wound compared to the physiological state (Fig 7c) and yielding sub-physiological values for  $\hat{H}$ . As shown in S2 Appendix, this leads the source term  $s_{\rho}$  to decrease when  $\Omega^{m}$  is increased if  $\rho \ge 1$ , as also reflected by the trends in Fig 7.

To capture the enhanced tissue fibrosis that would be expected when strengthening the mechano-biological coupling [23, 24], we revisit the definition of  $\hat{H}$  according to the widely accepted notion that stiffness can play a major role in regulating fibroblast activity [52, 81, 82]. Specifically, we assume that the mechanical parameter  $k_1$  provides a proxy of tissue stiffness, and adopt once again the same definition for  $\hat{H}_o$  and  $\hat{H}_o$ :

$$\hat{H} = \hat{H}(c, k_1^c, k_1^{ph}, \gamma^{k_1}) = \frac{c}{1 + exp\left(-\gamma^{k_1} \frac{k_1^c - k_1^{ph}}{k_1^{ph}}\right)},$$
(19)

where  $k_1^{ph} = k_1^{Skin}$  is the physiological value of  $k_1$ , *i.e.* that of unwounded skin,  $k_1^c$  is the local value of  $k_1$ , influenced by collagen deposition and crosslinking (Eq.(17)), and  $\gamma^{k_1}$  controls the slope of  $\hat{H}$  around its midpoint,  $k_1^c = k_1^{ph}$ , with a role analogous to that of  $\gamma^e$  in Eq.(10). Unlike Eqs.(10 and 19) also depends on c, linking the mechanosensitivity of cell proliferation and collagen deposition to ECM inflammation and reflecting the involvement of inflammatory pathways in tissue fibrosis [23].

As visible in Fig 8, the mechanobiological coupling encoded by Eq (19) induces a marked increase in  $\rho$ ,  $\phi_c$ , and  $\xi_c$  (Fig 8b, 8d and 8e and S5 Video) when the value of  $\Omega^m = \Omega_\rho^m = \Omega_{\phi_c}^m$  is increased, contrary to what observed in Fig 7. The higher cell density also yields larger active stresses and stronger ECM contraction (Fig 8c), enhancing the wound area reduction over time (Fig 8f and S5 Video) and causing faster depletion of the fibrin clot, which results in a more rapid decay of  $C_{10}$  (Fig 8g and S5 Video). Concomitantly, the increase in  $\phi_c$  and  $\xi_c$  determines a marked increase in  $k_1$  (Fig 8h and S5 Video) and a corresponding stiffening of the emergent mechanical behavior for a 21-day-old scar tissue (Fig 8i and S5 Video). Unlike for the previous mechanobiological coupling, the  $k_1$  increase resulting from a larger value of  $\Omega^m$ 

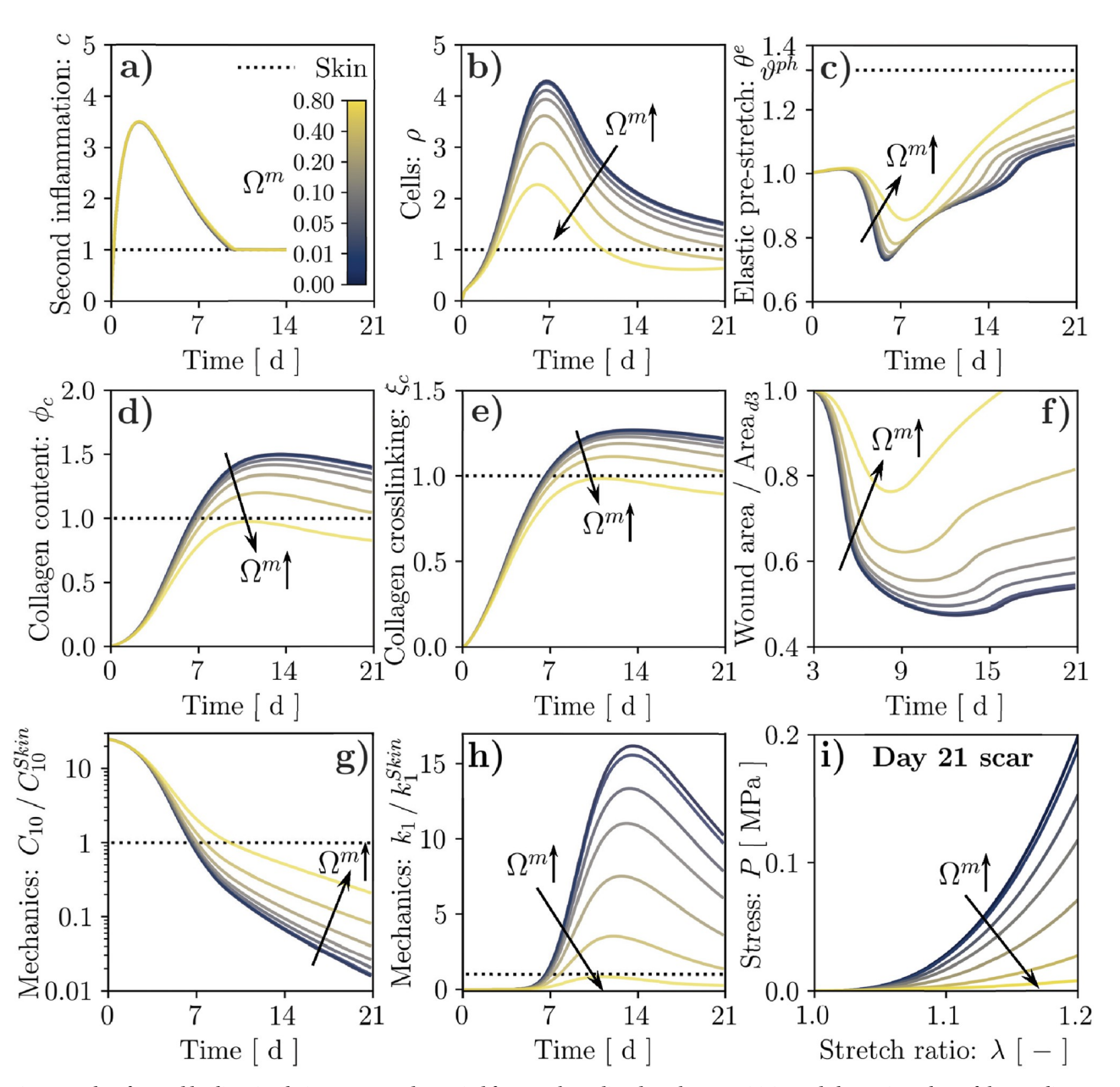


Fig 7. Results of wound healing simulation over a 21-day period for stretch-mediated mechanosensitivity and alternative values of the coupling strength, as controlled by the parameter  $\Omega^m$ . Temporal evolution of: second inflammatory signal, c, (a); cell population,  $\rho$ , (b); tissue elastic stretch,  $\theta^c$  (c); tissue collagen content,  $\phi_C$  (d); collagen crosslinking,  $\xi_C$  (e); wound area change (f); mechanical parameters  $C_{10}/C_{10}^{Skin}$  (g) and  $k_1/k_1^{Skin}$  (h). The wound healing outcome in terms of tissue mechanical behavior is visualized by evaluating its tensile response at day 21 post-wounding (i).

now triggers a positive feedback loop encoded by Eq (19). In fact, for the extreme case of  $\Omega^m = 0.8$  (S6 Video), this loop causes  $\rho$ ,  $\phi_c$ ,  $\xi_c$ , and thus  $k_1$ , to maintain sustained overexpression with respect to their physiological baseline values. This aspect is further analyzed in S3 Appendix, where we examine the equilibrium points of an ODE system derived from Eqs (67, 17–19), which can be considered representative of a 0-dimensional tissue region without biochemical field diffusion (Eq (3)) or remodeling (Eq (8)). Our analysis shows that  $\Omega^m$  affects the number of equilibrium points for the system, and setting  $\Omega^m = 0.8$  leads to a bi-stable system.

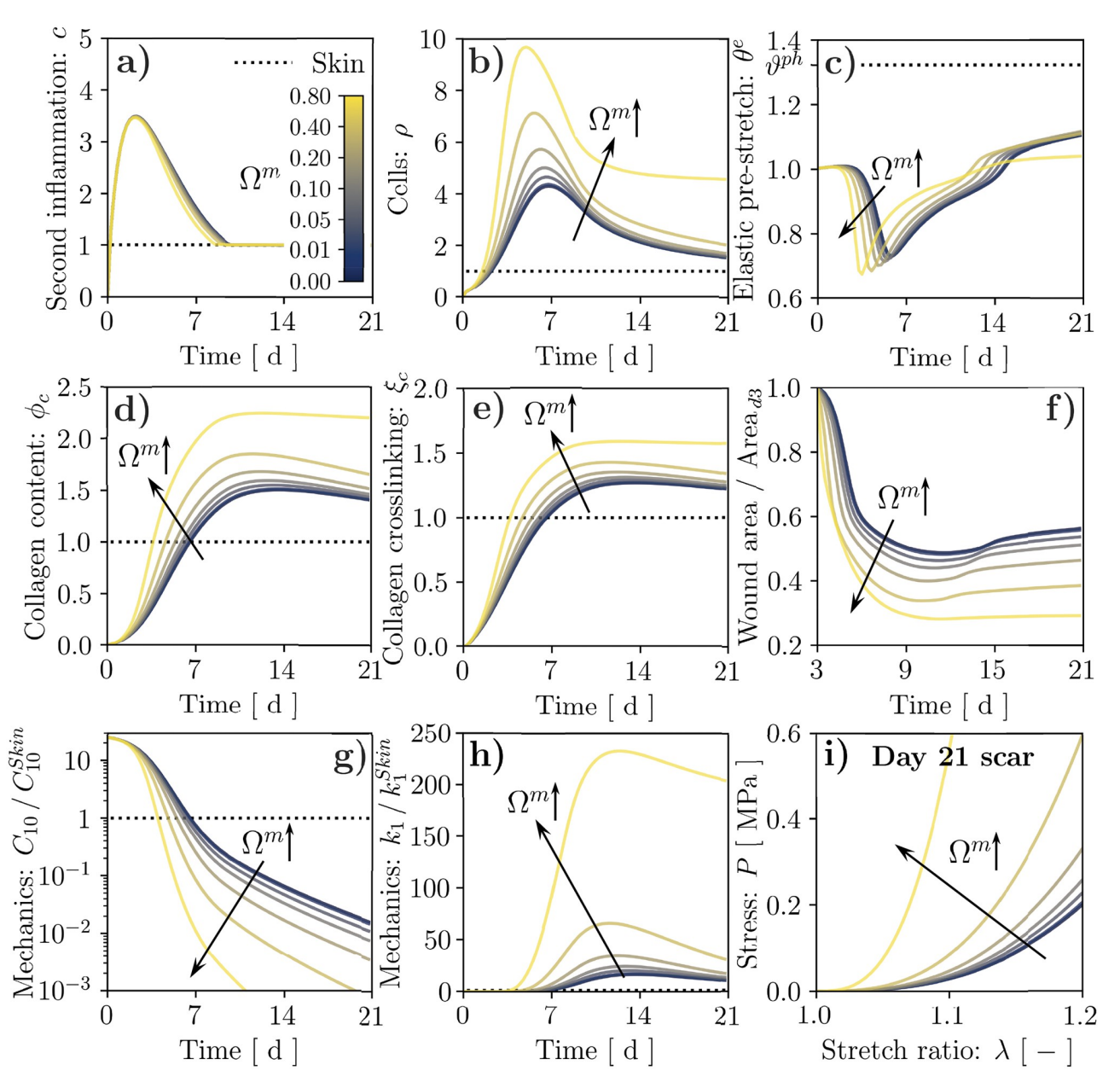


Fig 8. Results of wound healing simulation over a 21-day period for stiffness-mediated mechanosensitivity and alternative values of the coupling strength, as controlled by the parameter  $\Omega^m$ . Temporal evolution of: second inflammatory signal, c, (a); cell population,  $\rho$ , (b); tissue elastic stretch,  $\theta^c$  (c); tissue collagen content,  $\phi_c$ , (d); collagen crosslinking,  $\xi_c$ , (e); wound area change (f); mechanical parameters  $C_{10}/C_{10}^{Skin}$  (g) and  $k_1/k_1^{Skin}$  (h). The wound healing outcome in terms of tissue mechanical behavior is visualized by evaluating its tensile response at day 21 post-wounding (i).

Thus, the wound can reach a supra-physiological steady state, indicative of permanent fibrosis, while the surrounding unwounded tissue evolves towards the physiological steady state.

# **Discussion**

Computational models of cutaneous wound healing are gaining increasing popularity as promising tools in bioengineering and clinical contexts, *e.g.* personalized medicine [29, 83] and *in silico* clinical trials [84]. However, recent advances in the representation of the

biochemical processes underlying tissue repair have not been paralleled by similar developments in the description of the wound mechanics, mainly hindered by scant experimental evidence. In this study, we proposed to overcome these limitations by leveraging one of the very few available experimental datasets on the evolution of murine wound biomechanics throughout healing [41].

In order to determine constitutive model parameters for wounded and unwounded skin, and quantify their variability, we have established a novel hierarchical Bayesian inverse analysis procedure that is broadly applicable towards determining sets of inter-related, specimen-specific mechanical parameters from corresponding experimental data (Figs 2 and 4). Despite the large variability intrinsic to biological tissue properties, our approach allowed identifying overall trends for the wound constitutive parameters, highlighting clear softening of the non-collagenous ground substance throughout healing (Fig 4a) and sustained stiffening of the collagenous ECM with respect to the unwounded baseline (Fig 4b); we interpret the latter as indicative of wound/scar fibrosis.

Aiming to establish a versatile *in silico* tool to test alternative hypotheses on the biomechanical and mechano-biological pathways involved in wound healing, we then calibrated our systems-mechanobiological FE model [39, 42] to recapitulate the temporal evolution of several key biochemical and morphological aspects of murine wound healing over a 21-day period (Fig 5). Altering the tissue biomechanical parameters according to the 95% CI obtained from the Bayesian calibration procedure allowed us to assess their influence on the healing outcome in terms of wound permanent contracture and visible area changes. Specifically, we observed that softer/stiffer wounds develop into smaller/larger scars with reduced/increased permanent deformation (Fig 5), highlighting a cell-mediated mechanism whereby the wound ECM mechanics influences the outcome of the tissue repair processes.

Next, we used our model to propose bio-mechanical constitutive links for the emergent mechanical parameters of wounded tissue ( $C_{10}$ ,  $k_1$ ), starting from the underlying microstructural protein content ( $\phi_i^w$ ,  $\phi_c$ ), whose spatial and temporal evolution is determined by the biochemical  $(c, \rho)$  and mechanical  $(\theta^e, \theta^p)$  fields. In stark contrast with several previous works [36, 72-75], we found that a simple proportional relation between tissue stiffness and collagen content is unable to explain the changes in the mechanical parameters  $k_1$  that we derived from experimental data. Conversely, a nonlinear relation captures the strong increase and subsequent stabilization of  $k_1$  during the proliferation and remodeling stages of healing (Fig 6), and allows ascribing at least part of the experimental variability in  $k_1$  to potential specimen-specific differences in  $\phi_c$  and  $\xi_c$ . In line with previous works on the mechanics of collagen and actin networks, whose emergent response depends nonlinearly on crosslink density [85-87], our constitutive hypothesis was based on a power law, which we speculate to have a microstructural origin. Indeed, murine wound/scar tissue has been reported to feature an increased proportion of collagen crosslinks associated with fibrotic tissue with respect to the unwounded baseline [10, 88]. Similarly, the ratio between such crosslinks and those typical of soft connective tissues was upregulated in idiopathic pulmonary fibrosis, as were the density of mature crosslinks and the tissue stiffness, but not the collagen content [89]. Further supporting our modeling approach, the mature/immature crosslink ratio correlated positively with changes in the mechanical stiffness of lateral collateral ligament following injury [77], suggesting a dominant role of tissue 'quality' over its 'quantity' towards determining tissue fibrosis.

Lastly, we have leveraged our model to analyze the mechano-biological coupling from the mechanical state of the wound to the fibroblast proliferation and collagen deposition. In line with ubiquitous clinical evidence on the role of mechanical forces within tissue fibrosis [23–26], we expected that increasing this coupling would enhance cell infiltration, collagen

deposition, and thus increase  $k_1$  in the wound bed, ultimately exacerbating scar fibrosis. However, we found that a deformation-driven link between cell activity and the ECM mechanical state—supported by several works on stretch mechanosensitivity in fibroblasts [20, 21]—led to mitigated scarring, owing to the sub-physiological deformations of the wound ECM (Fig 7). On the other hand, extensive recent work in cell mechanobiology has highlighted a strong sensitivity of fibroblast activity to ECM stiffness [52, 81, 82, 90] through a pathway involving integrin-mediated adhesion [52, 91, 92], which we have also recently used to explain stretchmediated mechanosensitivity in cells by combining Bell's adhesion kinetics with the typical nonlinear strain-stiffening of collagenous ECMs [93]. Indeed, considering stiffness-driven cell mechanosensitivity (Fig 8) led all markers of tissue fibrosis included in our model ( $\phi_c$ ,  $\xi_c$ ,  $k_1$ ) to be overexpressed when increasing the coupling strength, suggesting that the nature of fibroblast mechanosensing and its involvement in wound healing remain open questions. Interestingly, for the strongest coupling that we considered ( $\Omega^m = 0.8$ ), the wound and the surrounding skin evolved towards different steady states, suggesting irreversible changes in the scar tissue. This result, obtained by analyzing bifurcations in the ODE system comprising the key evolution equations of our FE model (\$3 Appendix), matches the evidence that injured tissues can never regain the properties of native skin [10, 13–15].

This study explored several what if scenarios that challenge our fundamental understanding of the interplay between the biological, chemical and physical events involved in wound healing. However, it is not without limitations. First, while we have informed the model with experimental data, we have also neglected a few key aspects of wound healing. We focused on the evolving mechanics of the rebuilding dermal tissue, ignoring the role of keratinocytes within wound epithelialization and that of endothelial cells within angiogenesis. Both cell types are known to strongly affect the outcome of wound healing, e.g. by stimulating fibroblast function [18, 94], so that including them in our model would contribute to a broader and deeper understanding of the tissue repair process. Second, we have ignored any possible role of tissue anisotropy and three-dimensional geometries—both in the wound and in the surrounding skin—due to the lack of corresponding experimental information. Future experimental investigations of wound healing biomechanics should specifically address these aspects, providing invaluable quantitative data for further model developments. We have also considered a continuum representation of the tissues, which can provide an accurate description of their mechanics but is only one of the strategies for modeling wound healing. Since biological processes such as cell mechanosensing might be better captured by computational models at smaller scales, e.g. discrete fiber network and agent-based models, a natural future development of this work is to include a coupled multi-scale approach. Finally, a key result of this study is the proposition of a nonlinear link between the emergent mechanical response of the wound tissue and its collagen content. While this is not surprising, given the known network-like characteristics of collagenous tissues, the exponent a that we have used in Eq. (17)was selected arbitrarily and with the specific goal of matching the available experimental data. Future work should focus on including a physically-based link between the emergent mechanical behavior of the newly-formed collagenous networks and microstructural parameters such as the ratio between various collagen isoforms, the density, type, and kinetics of crosslinks, relevant network statistics (e.g. fiber diameters, stiffness, length between crosslinks), as well as the possible mechanical role of non-collagenous proteins (e.g. proteoglycans and glycoproteins).

#### Conclusion

Motivated by its potential relevance within bioengineering and clinical contexts, we have presented a calibrated systems-mechanobiological FE model of wound healing progression that

accounts, for the first time, for local changes in wounded tissue stiffness. The time-evolving mechanical characteristics of the repairing skin were inferred based on a novel, broadly applicable Bayesian inverse analysis procedure. The uncertainty propagation step following calibration allowed us to investigate the direct dependence between the local changes in wound stiffness and macroscopic contraction upon healing. The versatility of our model towards formulating and testing biomechanical and mechanobiological hypotheses was demonstrated by evaluating alternative links between the wound microstructural composition and its emergent mechanical behavior, as well as by discussing the implications of stretch-  $\nu s$ . stiffness-dominated mechanobiological coupling towards explaining the onset of irreversible scar fibrosis.

# **Supporting information**

S1 Fig. Convergence of ELBO for hierarchical Bayesian model calibrations. (PDF)

**S2** Fig. Hierarchical Bayesian model calibration for unwounded skin. (PDF)

S3 Fig. Hierarchical Bayesian model calibration for 7-day-old wounds. (PDF)

**S4** Fig. Hierarchical Bayesian model calibration for 14-day-old wounds. (PDF)

S1 Video. Simulation of wound healing progression with hard-coded mechanical parameters evolving linearly between the experimentally-informed median values, and stretch-driven mechanosensing with  $\Omega^m = 0.01$ .

(MP4)

S2 Video. Simulation of wound healing progression assuming that the mechanical parameter  $k_1$  depends linearly on the collagen content, and stretch-driven mechanosensing with  $\Omega^m = 0.01$ .

(MP4)

S3 Video. Simulation of wound healing progression assuming a power law linking the mechanical parameter  $k_1$  to the collagen content, and stretch-driven mechanosensing with  $\Omega^m = 0.01$ .

(MP4)

S4 Video. Simulation of wound healing progression assuming a power law linking the mechanical parameter  $k_1$  to the collagen content, and stretch-driven mechanosensing with  $\Omega^m = 0.08$ .

(MP4)

S5 Video. Simulation of wound healing progression assuming a power law linking the mechanical parameter  $k_1$  to the collagen content, and stiffness-driven mechanosensing with  $\Omega^m = 0.01$ .

(MP4)

S6 Video. Simulation of wound healing progression assuming a power law linking the mechanical parameter  $k_1$  to the collagen content, and stiffness-driven mechanosensing with  $\Omega^m = 0.08$ .

(MP4)

S1 Appendix. Literature data for wound biochemistry and mechanobiology. (PDF)

S2 Appendix. Sensitivity of  $s_{\rho}$  to  $\Omega^{m}$  for sub-physiological elastic stretch.

S3 Appendix. Equilibrium points for ODE system comprising Eqs (6, 7 and 18). (PDF)

S1 Table. Search ranges for Bayesian model parameters.

(PDF)

S2 Table. Global simulation parameters.

(PDF)

S3 Table. Parameters for diffusible biochemical fields.

(PDF)

S4 Table. Parameters for microstructural fields.

(PDF)

S5 Table. Emergent constitutive biomechanical parameters (Eqs (2, 16 and 17)). (PDF)

#### **Author Contributions**

Conceptualization: Marco Pensalfini, Adrian Buganza Tepole.

Data curation: Marco Pensalfini.

Formal analysis: Marco Pensalfini, Adrian Buganza Tepole.

Funding acquisition: Marco Pensalfini, Adrian Buganza Tepole.

Investigation: Marco Pensalfini, Adrian Buganza Tepole.

Methodology: Marco Pensalfini, Adrian Buganza Tepole.

**Project administration:** Adrian Buganza Tepole.

Resources: Adrian Buganza Tepole.

Software: Marco Pensalfini, Adrian Buganza Tepole.

Supervision: Adrian Buganza Tepole.

Validation: Marco Pensalfini, Adrian Buganza Tepole.

Visualization: Marco Pensalfini, Adrian Buganza Tepole.

Writing - original draft: Marco Pensalfini, Adrian Buganza Tepole.

Writing - review & editing: Marco Pensalfini, Adrian Buganza Tepole.

# References

- Martin P. Wound healing-aiming for perfect skin regeneration. Science. 1997; 276(5309):75–81. https://doi.org/10.1126/science.276.5309.75 PMID: 9082989
- Singer AJ, Clark RA. Cutaneous wound healing. New England journal of medicine. 1999; 341(10):738–746. https://doi.org/10.1056/NEJM199909023411006 PMID: 10471461

- Gurtner GC, Werner S, Barrandon Y, Longaker MT. Wound repair and regeneration. Nature. 2008; 453 (7193):314–321. https://doi.org/10.1038/nature07039 PMID: 18480812
- Su Y, Richmond A. Chemokine regulation of neutrophil infiltration of skin wounds. Advances in wound care. 2015; 4(11):631–640. https://doi.org/10.1089/wound.2014.0559 PMID: 26543677
- Delavary BM, van der Veer WM, van Egmond M, Niessen FB, Beelen RH. Macrophages in skin injury and repair. Immunobiology. 2011; 216(7):753–762. https://doi.org/10.1016/j.imbio.2011.01.001
- Turabelidze A, Dipietro LA. Inflammation and wound healing. Endodontic Topics. 2011; 24(1):26–38. https://doi.org/10.1111/etp.12012
- Barnes LA, Marshall CD, Leavitt T, Hu MS, Moore AL, Gonzalez JG, et al. Mechanical forces in cutaneous wound healing: emerging therapies to minimize scar formation. Advances in wound care. 2018; 7 (2):47–56. https://doi.org/10.1089/wound.2016.0709 PMID: 29392093
- Silver FH, Siperko LM, Seehra GP. Mechanobiology of force transduction in dermal tissue. Skin Research and Technology. 2003; 9(1):3–23. https://doi.org/10.1034/j.1600-0846.2003.00358.x PMID: 12535279
- Biggs LC, Kim CS, Miroshnikova YA, Wickström SA. Mechanical forces in the skin: roles in tissue architecture, stability, and function. Journal of Investigative Dermatology. 2020; 140(2):284–290. <a href="https://doi.org/10.1016/j.jid.2019.06.137">https://doi.org/10.1016/j.jid.2019.06.137</a> PMID: 31326398
- Wietecha MS, Pensalfini M, Cangkrama M, Müller B, Jin J, Brinckmann J, et al. Activin-mediated alterations of the fibroblast transcriptome and matrisome control the biomechanical properties of skin wounds. Nature communications. 2020; 11(1):1–20. <a href="https://doi.org/10.1038/s41467-020-16409-z">https://doi.org/10.1038/s41467-020-16409-z</a> PMID: 32451392
- Li B, Wang JHC. Fibroblasts and myofibroblasts in wound healing: force generation and measurement. Journal of tissue viability. 2011; 20(4):108–120. <a href="https://doi.org/10.1016/j.jtv.2009.11.004">https://doi.org/10.1016/j.jtv.2009.11.004</a> PMID: 19995679
- Van De Water L, Varney S, Tomasek JJ. Mechanoregulation of the myofibroblast in wound contraction, scarring, and fibrosis: opportunities for new therapeutic intervention. Advances in wound care. 2013; 2 (4):122–141. https://doi.org/10.1089/wound.2012.0393 PMID: 24527336
- Levenson S, Geever E, Crowley L, Oates J III, Berard C, Rosen H. Healing of rat skin wounds. Annals of surgery. 1965; 161(2):293.
- Doillon CJ, Dunn MG, Bender E, Silver FH. Collagen fiber formation in repair tissue: development of strength and toughness. Collagen and related research. 1985; 5(6):481–492. <a href="https://doi.org/10.1016/S0174-173X(85)80002-9">https://doi.org/10.1016/S0174-173X(85)80002-9</a> PMID: 3833451
- Corr DT, Gallant-Behm CL, Shrive NG, Hart DA. Biomechanical behavior of scar tissue and uninjured skin in a porcine model. Wound Repair and Regeneration. 2009; 17(2):250–259. https://doi.org/10. 1111/j.1524-475X.2009.00463.x PMID: 19320894
- Fife CE, Carter MJ. Wound care outcomes and associated cost among patients treated in US outpatient wound centers: data from the US wound registry. Wounds: a compendium of clinical research and practice. 2012; 24(1):10–17. PMID: 25875947
- Guest JF, Ayoub N, McIlwraith T, Uchegbu I, Gerrish A, Weidlich D, et al. Health economic burden that wounds impose on the National Health Service in the UK. BMJ open. 2015; 5(12):e009283. https://doi. org/10.1136/bmjopen-2015-009283 PMID: 26644123
- Guo Sa, DiPietro LA. Factors affecting wound healing. Journal of dental research. 2010; 89(3):219– 229. https://doi.org/10.1177/0022034509359125 PMID: 20139336
- Vogt PM, Andree C, Breuing K, Liu PY, Slama J, Helo G, et al. Dry, moist, and wet skin wound repair. Annals of plastic surgery. 1995; 34(5):493–9. https://doi.org/10.1097/00000637-199505000-00007 PMID: 7639486
- Wang JHC, Thampatty BP, Lin JS, Im HJ. Mechanoregulation of gene expression in fibroblasts. Gene. 2007; 391(1-2):1–15. https://doi.org/10.1016/j.gene.2007.01.014 PMID: 17331678
- Chiquet M, Gelman L, Lutz R, Maier S. From mechanotransduction to extracellular matrix gene expression in fibroblasts. Biochimica et Biophysica Acta (BBA)-Molecular Cell Research. 2009; 1793(5):911–920. https://doi.org/10.1016/j.bbamcr.2009.01.012 PMID: 19339214
- Agha R, Ogawa R, Pietramaggiori G, Orgill DP. A review of the role of mechanical forces in cutaneous wound healing. Journal of Surgical Research. 2011; 171(2):700–708. <a href="https://doi.org/10.1016/j.jss.2011.07.007">https://doi.org/10.1016/j.jss.2011.07.007</a> PMID: 22005503
- Wong VW, Rustad KC, Akaishi S, Sorkin M, Glotzbach JP, Januszyk M, et al. Focal adhesion kinase links mechanical force to skin fibrosis via inflammatory signaling. Nature medicine. 2012; 18(1):148– 152. https://doi.org/10.1038/nm.2574
- 24. Ma K, Kwon SH, Padmanabhan J, Duscher D, Trotsyuk AA, Dong Y, et al. Controlled delivery of a focal adhesion kinase inhibitor results in accelerated wound closure with decreased scar formation. Journal

- of Investigative Dermatology. 2018; 138(11):2452–2460. https://doi.org/10.1016/j.jid.2018.04.034 PMID: 29775632
- 25. Aarabi S, Bhatt KA, Shi Y, Paterno J, Chang EI, Loh SA, et al. Mechanical load initiates hypertrophic scar formation through decreased cellular apoptosis. The FASEB Journal. 2007; 21(12):3250–3261. https://doi.org/10.1096/fj.07-8218com PMID: 17504973
- Januszyk M, Wong VW, Bhatt KA, Vial IN, Paterno J, Longaker MT, et al. Mechanical offloading of incisional wounds is associated with transcriptional downregulation of inflammatory pathways in a large animal model. Organogenesis. 2014; 10(2):186–193. <a href="https://doi.org/10.4161/org.28818">https://doi.org/10.4161/org.28818</a> PMID: 24739276
- Wiegand C, White R. Microdeformation in wound healing. Wound Repair and Regeneration. 2013; 21 (6):793–799. https://doi.org/10.1111/wrr.12111 PMID: 24134318
- Huang C, Du Y, Ogawa R. Mechanobiology and Mechanotherapy for Cutaneous Wound-Healing. Mechanobiology: Exploitation for Medical Benefit. 2017; p. 239–253.
- Buganza Tepole A, Kuhl E. Systems-based approaches toward wound healing. Pediatric research. 2013; 73(2):553–563. https://doi.org/10.1038/pr.2013.3 PMID: 23314298
- Sherratt JA, Murray JD. Models of epidermal wound healing. Proceedings of the Royal Society of London Series B: Biological Sciences. 1990; 241(1300):29–36. <a href="https://doi.org/10.1098/rspb.1990.0061">https://doi.org/10.1098/rspb.1990.0061</a>
   PMID: 1978332
- Sherratt JA, Murray J. Mathematical analysis of a basic model for epidermal wound healing. Journal of mathematical biology. 1991; 29(5):389–404. https://doi.org/10.1007/BF00160468 PMID: 1831488
- Tranquillo RT, Murray J. Continuum model of fibroblast-driven wound contraction: inflammation-mediation. Journal of theoretical biology. 1992; 158(2):135–172. <a href="https://doi.org/10.1016/S0022-5193(05)80715-5">https://doi.org/10.1016/S0022-5193(05)80715-5</a> PMID: 1474841
- Cumming BD, McElwain D, Upton Z. A mathematical model of wound healing and subsequent scarring. Journal of The Royal Society Interface. 2010; 7(42):19–34. https://doi.org/10.1098/rsif.2008.0536 PMID: 19324672
- Valero C, Javierre E, García-Aznar J, Gómez-Benito M, Menzel A. Modeling of anisotropic wound healing. Journal of the Mechanics and Physics of Solids. 2015; 79:80–91. <a href="https://doi.org/10.1016/j.jmps.2015.03.009">https://doi.org/10.1016/j.jmps.2015.03.009</a>
- Olsen L, Sherratt JA, Maini PK. A mechanochemical model for adult dermal wound contraction and the permanence of the contracted tissue displacement profile. Journal of theoretical biology. 1995; 177 (2):113–128. https://doi.org/10.1006/jtbi.1995.0230 PMID: 8558902
- Valero C, Javierre E, García-Aznar JM, Gómez-Benito MJ. A cell-regulatory mechanism involving feed-back between contraction and tissue formation guides wound healing progression. PloS one. 2014; 9 (3):e92774. https://doi.org/10.1371/journal.pone.0092774 PMID: 24681636
- Bowden L, Byrne H, Maini P, Moulton D. A morphoelastic model for dermal wound closure. Biomechanics and modeling in mechanobiology. 2016; 15(3):663–681. <a href="https://doi.org/10.1007/s10237-015-0716-7">https://doi.org/10.1007/s10237-015-0716-7</a>
   PMID: 26264498
- Buganza Tepole A, Kuhl E. Computational modeling of chemo-bio-mechanical coupling: a systems-biology approach toward wound healing. Computer methods in biomechanics and biomedical engineering. 2016; 19(1):13–30. https://doi.org/10.1080/10255842.2014.980821 PMID: 25421487
- **39.** Buganza Tepole A. Computational systems mechanobiology of wound healing. Computer Methods in Applied Mechanics and Engineering. 2017; 314:46–70. https://doi.org/10.1016/j.cma.2016.04.034
- Sohutskay DO, Buganza Tepole A, Voytik-Harbin SL. Mechanobiological wound model for improved design and evaluation of collagen dermal replacement scaffolds. Acta Biomaterialia. 2021; 135:368– 382. https://doi.org/10.1016/j.actbio.2021.08.007 PMID: 34390846
- Pensalfini M, Haertel E, Hopf R, Wietecha M, Werner S, Mazza E. The mechanical fingerprint of murine excisional wounds. Acta Biomaterialia. 2018; 65:226–236. <a href="https://doi.org/10.1016/j.actbio.2017.10.021">https://doi.org/10.1016/j.actbio.2017.10.021</a> PMID: 29031511
- **42.** Pensalfini M, Buganza Tepole A. Wound Healing Mechanobiology; 2022. Available from: <a href="https://bitbucket.org/buganzalab/workspace/projects/WHM">https://bitbucket.org/buganzalab/workspace/projects/WHM</a>.
- Loerakker S, Ristori T, Baaijens FP. A computational analysis of cell-mediated compaction and collagen remodeling in tissue-engineered heart valves. Journal of the Mechanical Behavior of Biomedical Materials. 2016; 58:173–187. https://doi.org/10.1016/j.jmbbm.2015.10.001 PMID: 26608336
- Gasser TC, Ogden RW, Holzapfel GA. Hyperelastic modelling of arterial layers with distributed collagen fibre orientations. Journal of the royal society interface. 2006; 3(6):15–35. <a href="https://doi.org/10.1098/rsif.2005.0073">https://doi.org/10.1098/rsif.2005.0073</a> PMID: 16849214
- **45.** Sommer G, Eder M, Kovacs L, Pathak H, Bonitz L, Mueller C, et al. Multiaxial mechanical properties and constitutive modeling of human adipose tissue: a basis for preoperative simulations in plastic and

- reconstructive surgery. Acta biomaterialia. 2013; 9(11):9036–9048. https://doi.org/10.1016/j.actbio. 2013.06.011 PMID: 23811521
- 46. Tonge TK, Voo LM, Nguyen TD. Full-field bulge test for planar anisotropic tissues: Part II–A thin shell method for determining material parameters and comparison of two distributed fiber modeling approaches. Acta biomaterialia. 2013; 9(4):5926–5942. https://doi.org/10.1016/j.actbio.2012.11.034 PMID: 23220451
- Bajuri M, Isaksson H, Eliasson P, Thompson MS. A hyperelastic fibre-reinforced continuum model of healing tendons with distributed collagen fibre orientations. Biomechanics and modeling in mechanobiology. 2016; 15(6):1457–1466. https://doi.org/10.1007/s10237-016-0774-5 PMID: 26951049
- Aldieri A, Terzini M, Bignardi C, Zanetti EM, Audenino AL. Implementation and validation of constitutive relations for human dermis mechanical response. Medical & Biological Engineering & Computing. 2018; 56(11):2083–2093. https://doi.org/10.1007/s11517-018-1843-y PMID: 29777504
- 49. Puértolas S, Peña E, Herrera A, Ibarz E, Gracia L. A comparative study of hyperelastic constitutive models for colonic tissue fitted to multiaxial experimental testing. Journal of the mechanical behavior of biomedical materials. 2020; 102:103507. https://doi.org/10.1016/j.jmbbm.2019.103507 PMID: 31877516
- Moreo P, García-Aznar JM, Doblaré M. Modeling mechanosensing and its effect on the migration and proliferation of adherent cells. Acta biomaterialia. 2008; 4(3):613–621. <a href="https://doi.org/10.1016/j.actbio.2007.10.014">https://doi.org/10.1016/j.actbio.2007.10.014</a> PMID: 18180207
- Han YP, Tuan TL, Hughes M, Wu H, Garner WL. Transforming growth factor-β-and tumor necrosis factor-α-mediated induction and proteolytic activation of MMP-9 in human skin. Journal of Biological Chemistry. 2001; 276(25):22341–22350. https://doi.org/10.1074/jbc.M010839200 PMID: 11297541
- Humphrey JD, Dufresne ER, Schwartz MA. Mechanotransduction and extracellular matrix homeostasis. Nature reviews Molecular cell biology. 2014; 15(12):802–812. <a href="https://doi.org/10.1038/nrm3896">https://doi.org/10.1038/nrm3896</a>
   PMID: 25355505
- 53. Weickenmeier J, Jabareen M, Mazza E. Suction based mechanical characterization of superficial facial soft tissues. Journal of biomechanics. 2015; 48(16):4279–4286. <a href="https://doi.org/10.1016/j.jbiomech.2015.10.039">https://doi.org/10.1016/j.jbiomech.2015.10.039</a> PMID: 26584965
- Pensalfini M, Rotach M, Hopf R, Bielicki A, Santoprete R, Mazza E. How cosmetic tightening products modulate the biomechanics and morphology of human skin. Acta biomaterialia. 2020; 115:299–316. https://doi.org/10.1016/j.actbio.2020.08.027 PMID: 32853810
- 55. Groves RB, Coulman SA, Birchall JC, Evans SL. An anisotropic, hyperelastic model for skin: experimental measurements, finite element modelling and identification of parameters for human and murine skin. Journal of the mechanical behavior of biomedical materials. 2013; 18:167–180. <a href="https://doi.org/10.1016/j.jmbbm.2012.10.021">https://doi.org/10.1016/j.jmbbm.2012.10.021</a> PMID: 23274398
- 56. Meador WD, Sugerman GP, Story HM, Seifert AW, Bersi MR, Tepole AB, et al. The regional-dependent biaxial behavior of young and aged mouse skin: A detailed histomechanical characterization, residual strain analysis, and constitutive model. Acta biomaterialia. 2020; 101:403–413. https://doi.org/10.1016/j.actbio.2019.10.020 PMID: 31614209
- Blei DM, Kucukelbir A, McAuliffe JD. Variational inference: A review for statisticians. Journal of the American statistical Association. 2017; 112(518):859–877. <a href="https://doi.org/10.1080/01621459.2017.1285773">https://doi.org/10.1080/01621459.2017.1285773</a>
- Salvatier J, Wiecki TV, Fonnesbeck C. Probabilistic programming in Python using PyMC3. PeerJ Computer Science. 2016; 2:e55. https://doi.org/10.7717/peerj-cs.55
- **59.** Kucukelbir A, Tran D, Ranganath R, Gelman A, Blei DM. Automatic differentiation variational inference. Journal of machine learning research. 2017;.
- 60. Dauendorffer J, Bastuji-Garin S, Guéro S, Brousse N, Fraitag S. Shrinkage of skin excision specimens: formalin fixation is not the culprit. British Journal of Dermatology. 2009; 160(4):810–814. <a href="https://doi.org/10.1111/j.1365-2133.2008.08994.x">https://doi.org/10.1111/j.1365-2133.2008.08994.x</a> PMID: 19183182
- Upchurch DA, Malenfant RC, Wignall JR, Ogden DM, Saile K. Effects of sample site and size, skin tension lines, surgeon, and formalin fixation on shrinkage of skin samples excised from canine cadavers.
   American journal of veterinary research. 2014; 75(11):1004–1009. <a href="https://doi.org/10.2460/ajvr.75.11">https://doi.org/10.2460/ajvr.75.11</a>.
   1004 PMID: 25350091
- 62. Reynolds L, Conti F, Lucas M, Grose R, Robinson S, Stone M, et al. Accelerated re-epithelialization in β3-integrin-deficient-mice is associated with enhanced TGF-β1 signaling. Nature medicine. 2005; 11 (2):167–174. https://doi.org/10.1038/nm1165 PMID: 15654327
- **63.** Komi-Kuramochi A, Kawano M, Oda Y, Asada M, Suzuki M, Oki J, et al. Expression of fibroblast growth factors and their receptors during full-thickness skin wound healing in young and aged mice. Journal of Endocrinology. 2005; 186(2):273–289. https://doi.org/10.1677/joe.1.06055 PMID: 16079254

- 64. Wang XJ, Han G, Owens P, Siddiqui Y, Li AG. Role of TGFβ-mediated inflammation in cutaneous wound healing. Journal of Investigative Dermatology Symposium Proceedings. 2006; 11(1):112–117. https://doi.org/10.1038/sj.jidsymp.5650004 PMID: 17069018
- Ishida Y, Gao JL, Murphy PM. Chemokine receptor CX3CR1 mediates skin wound healing by promoting macrophage and fibroblast accumulation and function. The Journal of Immunology. 2008; 180 (1):569–579. https://doi.org/10.4049/jimmunol.180.1.569 PMID: 18097059
- Schmidt BA, Horsley V. Intradermal adipocytes mediate fibroblast recruitment during skin wound healing. Development. 2013; 140(7):1517–1527. https://doi.org/10.1242/dev.087593 PMID: 23482487
- DiPietro LA, Burdick M, Low QE, Kunkel SL, Strieter RM, et al. MIP-1alpha as a critical macrophage chemoattractant in murine wound repair. The Journal of clinical investigation. 1998; 101(8):1693–1698. https://doi.org/10.1172/JCI1020 PMID: 9541500
- 68. Low QE, Drugea IA, Duffner LA, Quinn DG, Cook DN, Rollins BJ, et al. Wound healing in MIP-1α-/- and MCP-1-/- mice. The American journal of pathology. 2001; 159(2):457–463. https://doi.org/10.1016/s0002-9440(10)61717-8 PMID: 11485904
- Egozi EI, Ferreira AM, Burns AL, Gamelli RL, Dipietro LA. Mast cells modulate the inflammatory but not the proliferative response in healing wounds. Wound Repair and Regeneration. 2003; 11(1):46–54. https://doi.org/10.1046/j.1524-475X.2003.11108.x PMID: 12581426
- Dovi JV, He LK, DiPietro LA. Accelerated wound closure in neutrophil-depleted mice. Journal of leukocyte biology. 2003; 73(4):448–455. https://doi.org/10.1189/jlb.0802406 PMID: 12660219
- Yang G, Crawford RC, Wang JH. Proliferation and collagen production of human patellar tendon fibroblasts in response to cyclic uniaxial stretching in serum-free conditions. Journal of biomechanics. 2004; 37(10):1543–1550. https://doi.org/10.1016/j.jbiomech.2004.01.005 PMID: 15336929
- Baaijens F, Bouten C, Driessen N. Modeling collagen remodeling. Journal of biomechanics. 2010; 43 (1):166–175. https://doi.org/10.1016/j.jbiomech.2009.09.022 PMID: 19818962
- Loerakker S, Obbink-Huizer C, Baaijens F. A physically motivated constitutive model for cell-mediated compaction and collagen remodeling in soft tissues. Biomechanics and modeling in mechanobiology. 2014; 13(5):985–1001. https://doi.org/10.1007/s10237-013-0549-1 PMID: 24370853
- Rouillard AD, Holmes JW. Coupled agent-based and finite-element models for predicting scar structure following myocardial infarction. Progress in biophysics and molecular biology. 2014; 115(2-3):235–243. https://doi.org/10.1016/j.pbiomolbio.2014.06.010 PMID: 25009995
- 75. Zhuan X, Luo X, Gao H, Ogden RW. Coupled agent-based and hyperelastic modelling of the left ventricle post-myocardial infarction. International journal for numerical methods in biomedical engineering. 2019; 35(1):e3155. https://doi.org/10.1002/cnm.3155 PMID: 30253447
- Lee YU, Lee A, Humphrey J, Rausch M. Histological and biomechanical changes in a mouse model of venous thrombus remodeling. Biorheology. 2015; 52(3):235–245. https://doi.org/10.3233/BIR-15058 PMID: 26444224
- 77. Dunham CL, Steenbock H, Brinckmann J, Reiter AJ, Castile RM, Chamberlain AM, et al. Increased volume and collagen crosslinks drive soft tissue contribution to post-traumatic elbow contracture in an animal model. Journal of Orthopaedic Research. 2021; 39(8):1800–1810. <a href="https://doi.org/10.1002/jor.24781">https://doi.org/10.1002/jor.24781</a> PMID: 33258516
- 78. Yoshida K, Jiang H, Kim M, Vink J, Cremers S, Paik D, et al. Quantitative evaluation of collagen crosslinks and corresponding tensile mechanical properties in mouse cervical tissue during normal pregnancy. PloS one. 2014; 9(11):e112391. https://doi.org/10.1371/journal.pone.0112391 PMID: 25397407
- Malandrino A, Trepat X, Kamm RD, Mak M. Dynamic filopodial forces induce accumulation, damage, and plastic remodeling of 3D extracellular matrices. PLoS computational biology. 2019; 15(4): e1006684. https://doi.org/10.1371/journal.pcbi.1006684 PMID: 30958816
- DeGroot J. The AGE of the matrix: chemistry, consequence and cure. Current opinion in pharmacology. 2004; 4(3):301–305. https://doi.org/10.1016/j.coph.2004.01.007 PMID: 15140424
- 81. Hadjipanayi E, Mudera V, Brown R. Close dependence of fibroblast proliferation on collagen scaffold matrix stiffness. Journal of tissue engineering and regenerative medicine. 2009; 3(2):77–84. https://doi. org/10.1002/term.136 PMID: 19051218
- Smith PC, Martínez C, Martínez J, McCulloch CA. Role of fibroblast populations in periodontal wound healing and tissue remodeling. Frontiers in physiology. 2019; 10:270. <a href="https://doi.org/10.3389/fphys.2019.00270">https://doi.org/10.3389/fphys.2019.00270</a> PMID: 31068825
- 83. Peng GC, Alber M, Buganza Tepole A, Cannon WR, De S, Dura-Bernal S, et al. Multiscale modeling meets machine learning: What can we learn? Archives of Computational Methods in Engineering. 2021; 28(3):1017–1037. https://doi.org/10.1007/s11831-020-09405-5 PMID: 34093005

- 84. Pappalardo F, Russo G, Tshinanu FM, Viceconti M. In silico clinical trials: concepts and early adoptions. Briefings in bioinformatics. 2019; 20(5):1699–1708. <a href="https://doi.org/10.1093/bib/bby043">https://doi.org/10.1093/bib/bby043</a> PMID: 29868882
- 85. Gardel M, Shin JH, MacKintosh F, Mahadevan L, Matsudaira P, Weitz DA. Elastic behavior of cross-linked and bundled actin networks. Science. 2004; 304(5675):1301–1305. https://doi.org/10.1126/science.1095087 PMID: 15166374
- 86. Zagar G, Onck PR, Van der Giessen E. Elasticity of rigidly cross-linked networks of athermal filaments. Macromolecules. 2011; 44(17):7026–7033. https://doi.org/10.1021/ma201257v
- Lin S, Gu L. Influence of crosslink density and stiffness on mechanical properties of type I collagen gel. Materials. 2015; 8(2):551–560. https://doi.org/10.3390/ma8020551 PMID: 28787956
- 88. Knipper JA, Willenborg S, Brinckmann J, Bloch W, Maaß T, Wagener R, et al. Interleukin-4 receptor α signaling in myeloid cells controls collagen fibril assembly in skin repair. Immunity. 2015; 43(4):803–816. https://doi.org/10.1016/j.immuni.2015.09.005 PMID: 26474656
- 89. Jones MG, Andriotis OG, Roberts JJ, Lunn K, Tear VJ, Cao L, et al. Nanoscale dysregulation of collagen structure-function disrupts mechano-homeostasis and mediates pulmonary fibrosis. Elife. 2018; 7: e36354. https://doi.org/10.7554/eLife.36354 PMID: 29966587
- Chen K, Kwon SH, Henn D, Kuehlmann BA, Tevlin R, Bonham CA, et al. Disrupting biological sensors
  of force promotes tissue regeneration in large organisms. Nature communications. 2021; 12(1):1–15.
  <a href="https://doi.org/10.1038/s41467-021-25410-z">https://doi.org/10.1038/s41467-021-25410-z</a> PMID: 34489407
- 91. Sun Z, Guo SS, Fässler R. Integrin-mediated mechanotransduction. Journal of Cell Biology. 2016; 215 (4):445–456. https://doi.org/10.1083/jcb.201609037 PMID: 27872252
- 92. Mascharak S, desJardins Park HE, Davitt MF, Griffin M, Borrelli MR, Moore AL, et al. Preventing Engrailed-1 activation in fibroblasts yields wound regeneration without scarring. Science. 2021; 372 (6540):eaba2374. https://doi.org/10.1126/science.aba2374 PMID: 33888614
- 93. Guo Y, Calve S, Buganza Tepole A. Multiscale mechanobiology: coupling models of adhesion kinetics and nonlinear tissue mechanics. Biophysical Journal. 2022;. <a href="https://doi.org/10.1016/j.bpj.2022.01.012">https://doi.org/10.1016/j.bpj.2022.01.012</a> PMID: 35074393
- 94. Werner S, Krieg T, Smola H. Keratinocyte–fibroblast interactions in wound healing. Journal of investigative dermatology. 2007; 127(5):998–1008. https://doi.org/10.1038/sj.jid.5700786 PMID: 17435785